



Hyper Suprime-Cam: System design and verification of image quality

Satoshi MIYAZAKI,^{1,2,*} Yutaka KOMIYAMA,^{1,2} Satoshi KAWANOMOTO,¹
 Yoshiyuki DOI,¹ Hisanori FURUSAWA,¹ Takashi HAMANA,¹ Yusuke HAYASHI,¹
 Hiroyuki IKEDA,¹ Yukiko KAMATA,¹ Hiroshi KAROJI,¹ Michitaro KOIKE,¹
 Tomio KURAKAMI,¹ Shoken MIYAMA,^{1,3} Tomoki MOROKUMA,^{1,4}
 Fumiaki NAKATA,¹ Kazuhito NAMIKAWA,¹ Hidehiko NAKAYA,¹ Kyoji NARIAI,¹
 Yoshiyuki OBUCHI,¹ Yukie OISHI,¹ Norio OKADA,¹ Yuki OKURA,¹ Philip TAIT,¹
 Tadafumi TAKATA,¹ Yoko TANAKA,¹ Masayuki TANAKA,¹ Tsuyoshi TERAI,¹
 Daigo TOMONO,¹ Fumihiro Uraguchi,¹ Tomonori USUDA,¹ Yousuke UTSUMI,³
 Yoshihiko YAMADA,¹ Hitomi YAMANOI,¹ Hiroaki AIHARA,^{5,6} Hiroki FUJIMORI,⁵
 Sogo MINEO,^{1,5} Hironao MIYATAKE,^{6,7,8} Masamune OGURI,⁵
 Tomohisa UCHIDA,⁹ Manobu M. TANAKA,^{9,10} Naoki YASUDA,⁶
 Masahiro TAKADA,⁶ Hitoshi MURAYAMA,⁶ Atsushi J. NISHIZAWA,¹¹
 Naoshi SUGIYAMA,¹¹ Masashi CHIBA,¹² Toshifumi FUTAMASE,^{12,13}
 Shiang-Yu WANG,¹⁴ Hsin-Yo CHEN,¹⁴ Paul T. P. Ho,¹⁴ Eric J. Y. LIAW,¹⁵
 Chi-Fang CHIU,¹⁵ Cheng-Lin HO,¹⁵ Tsang-Chih LAI,¹⁵ Yao-Cheng LEE,¹⁵
 Dun-Zen JENG,¹⁵ Satoru IWAMURA,¹⁶ Robert ARMSTRONG,⁷
 Steve BICKERTON,^{6,7} James BOSCH,⁷ James E. GUNN,⁷ Robert H. LUPTON,⁷
 Craig LOOMIS,⁷ Paul PRICE,⁷ Steward SMITH,⁷ Michael A. STRAUSS,⁷
 Edwin L. TURNER,^{6,7} Hisanori SUZUKI,¹⁷ Yasuhito MIYAZAKI,¹⁷
 Masaharu MURAMATSU,¹⁷ Koei YAMAMOTO,¹⁷ Makoto ENDO,¹⁸ Yutaka EZAKI,¹⁸
 Noboru ITO,¹⁸ Noboru KAWAGUCHI,¹⁸ Satoshi SOFUKU,¹⁸ Tomoaki TANIIKE,¹⁸
 Kotaro AKUTSU,¹⁹ Naoto DOJO,¹⁹ Kazuyuki KASUMI,¹⁹ Toru MATSUDA,¹⁹
 Kohei IMOTO,¹⁹ Yoshinori MIWA,¹⁹ Masayuki SUZUKI,¹⁹ Kunio TAKESHI,²⁰
 and Hideo YOKOTA¹⁹

¹National Astronomical Observatory of Japan, 2-21-1 Osawa, Mitaka, Tokyo 181-8588, Japan

²Department of Astronomical Science, SOKENDAI (The Graduate University for Advanced Studies), 2-21-1 Osawa, Mitaka, Tokyo 181-8588, Japan

³Hiroshima University, 1-3-1 Kagamiyama, Higashi-Hiroshima, Hiroshima 739-8526, Japan

⁴Institute of Astronomy, The University of Tokyo, 2-21-1 Osawa, Mitaka, Tokyo 181-0015, Japan

⁵Department of Physics, The University of Tokyo, 7-3-1 Hongo, Bunkyo-ku, Tokyo 113-0033, Japan

⁶Kavli Institute for the Physics and Mathematics of the Universe (Kavli IPMU, WPI), The University of Tokyo, 5-1-5 Kashiwa-no-Ha, Kashiwa, Chiba 277-8582, Japan

⁷Princeton University Observatory, 4 Ivy Ln, Princeton, NJ 08544-1001, USA

⁸Jet Propulsion Laboratory, 4800 Oak Grove Drive, Pasadena, CA 91109, USA

⁹Institute of Particle and Nuclear Studies, High Energy Accelerator Research Organization (KEK), 1-1 Oho, Tsukuba, Ibaraki 305-0801, Japan

¹⁰Department of Particle and Nuclear Physics, The Graduate University for Advanced Studies, 1-1 Oho, Tsukuba, Ibaraki 305-0801, Japan

¹¹Institute for Advanced Research, Nagoya University, Furo-cho, Chikusa-ku, Nagoya, Aichi 464-8602, Japan

¹²Tohoku University, 6-3 Aoba, Aramaki, Aoba-ku, Sendai, Miyagi 980-8578, Japan

¹³Kyoto Sangyo University, Motoyama, Kamigamo, Kita-Ku, Kyoto, Kyoto 603-8555, Japan

¹⁴Institute of Astronomy and Astrophysics, Academia Sinica, No.1, Sec. 4, Roosevelt Rd, Taipei 10617, Taiwan, R.O.C.

¹⁵Aeronautical System Research Division, Chung Shan Institute of Science and Technology, No. 300-5, Ln. 277, Xi-an St., Xitun Dist., Taichung 40722, Taiwan, R.O.C.

¹⁶MRJ, 2-16-2 Kugenuma-Kaigan, Fujisawa, Kanagawa 251-0037, Japan

¹⁷Hamamatsu Photonics, 1126-1, Ichino-cho, Higashi-ku, Hamamatsu, Shizuoka 435-8558, Japan

¹⁸Mitsubishi Electric, 8-1-1 Tsukaguchi-Honmachi, Amagasaki, Hyogo 661-0001, Japan

¹⁹Canon, 19-1 Kiyohara Industrial Park, Utsunomiya, Tochigi 321-3293, Japan

²⁰Okamoto Optics, 8-34 Haramachi, Isogo-ku, Yokohama, Kanagawa 235-0008, Japan

*E-mail: satoshi@nao.j.org

Received 2017 May 18; Accepted 2017 June 21

Abstract

The Hyper Suprime-Cam (HSC) is an 870 megapixel prime focus optical imaging camera for the 8.2 m Subaru telescope. The wide-field corrector delivers sharp images of $0.^{\prime\prime}2$ (FWHM) in the HSC-*i* band over the entire $1.^{\circ}5$ diameter field of view. The collimation of the camera with respect to the optical axis of the primary mirror is done with hexapod actuators, the mechanical accuracy of which is a few microns. Analysis of the remaining wavefront error in off-focus stellar images reveals that the collimation of the optical components meets design specifications. While there is a flexure of mechanical components, it also is within the design specification. As a result, the camera achieves its seeing-limited imaging on Maunakea during most of the time; the median seeing over several years of observing is $0.^{\prime\prime}67$ (FWHM) in the *i* band. The sensors use p-channel, fully depleted CCDs of $200\text{ }\mu\text{m}$ thickness (2048×4176 $15\text{ }\mu\text{m}$ square pixels) and we employ 116 of them to pave the 50 cm diameter focal plane. The minimum interval between exposures is 34 s, including the time to read out arrays, to transfer data to the control computer, and to save them to the hard drive. HSC on Subaru uniquely features a combination of a large aperture, a wide field of view, sharp images and a high sensitivity especially at longer wavelengths, which makes the HSC one of the most powerful observing facilities in the world.

Key words: instrumentation: detectors — techniques: image processing — telescopes

1 Introduction

Imaging at visible wavelengths is one of the oldest observing styles in astronomy, but it still plays a key roles in many frontier research areas. The demands on imaging survey speed, which can be quantified as the product of the area of the primary mirror, A [m^2], and the field of view of the camera, Ω [deg^2], have become even larger since the discovery of the cosmic acceleration using Type Ia supernovae (SNIa) (Perlmutter et al. 1998; Riess et al. 1998). Large-scale visible light surveys have been planned in the

context of cosmological studies to understand the origin of this acceleration. Weak lensing (WL) is another promising probe for the study of the distribution of dark matter and of the nature of dark energy. This requires that the shapes of large numbers of distant galaxies are accurately measured (Weinberg et al. 2013). Thus, the observing targets are faint, small in angular size, and widely spread out over the sky. Therefore, a high angular resolution imager with large survey speed is crucial for cosmological surveys.

Large-aperture telescopes that have ~ 4 m primary mirrors usually have a Ritchey–Chrétien (R–C) design in which a combination of the hyperbolic primary and the (convex) secondary eliminates the spherical and comatic aberrations. The alternative prime focus of a telescope has the shortest focal length and therefore provides a wide field of view (FOV). However, rays reflected from a single hyperbolic primary suffer from various types of aberrations, even at the optical center. Wynne (1968) was the first to design a three-lens corrector for the prime focus of an R–C hyperboloid mirror. In his design for the Kitt Peak National Observatory 4 m Mayall telescope, all the surfaces are spherical and only UBK7 is used as a glass material. By correcting for spherical aberration, coma, astigmatism, and field distortion, the image spread, s , is smaller than $0''.5$ over a $30'$ diameter FOV, and $s < 1''.0$ over a $50'$ diameter FOV. However, this design only works over a narrow wavelength coverage, 400–500 nm, which is much smaller than today's standards.

Even larger telescopes (8–10 m) typically have faster primary mirrors ($F \lesssim 2$), which makes the design of a prime focus corrector challenging. There has also been an increasing demand for a broad wavelength coverage, which calls for the introduction of an atmospheric dispersion corrector (ADC). Nariai, Yamashita, and Nakagiri (1985) designed a corrector for the $F/2$ primary focus of the Subaru telescope and realized an image diameter of $0''.2$. They carefully determined the positions of three lenses to balance the chromatic aberration and the image quality at the edge of the field. They proposed several variants of the design in response to changes in the telescope design and ended up with a design where they employed fluorine phosphor glass (OHARA FPL51) for the triplet to minimize the chromatic aberrations (Nariai 1992). Takeshi (2000) refined the design by replacing the first two FPL51 glasses with OHARA BSL7 (Schott BK7 equivalent), which is easier to manufacture. The obvious drawback was the increase of chromatic aberrations, but this was reduced by relocating the first lens closer to the focal plane. This also reduced the size of the lens to a diameter of 0.5 m. In addition, Takeshi (2000) invented a novel lateral shift ADC (section 3). These breakthroughs enabled the actual fabrication of a corrector for Subaru (Yokota 2001), and realized the wide-field prime focus imaging on an 8 m class telescope for the first time.

As a telescope becomes larger, the focal plane becomes larger compared with the typical dimensions of CCD detectors. Therefore, CCDs have been configured in mosaics to cover the large focal plane. One of the pioneering works was done by Sekiguchi et al. (1992) who employed commercial 1000×1018 pixel CCDs (12 μm square pixel, TC215 developed by TI Japan) and put them into a 2×8 configuration to have 2000×8144 pixels in total. The camera was

mounted on the 1.3 m Kiso Schmidt telescope. Each array has custom-machined aluminum nitride (AlN) base spacer epoxied from the back to approximately follow the spherical focal surface of the Schmidt telescope. The focus error is measured to be less than $40 \mu\text{m}$. Although the spacing between the devices in this camera is large and comparable to the dimension of the imaging area, this mosaic camera had the widest photosensitive area of any CCD camera to date.

The Sloan Digital Sky Survey Photometric Camera (Gunn et al. 1998) realized an even larger focal plane by employing $30 \times 2048 \times 2048$ (24 μm pixels) SITe/Tektronix CCDs. Because the 2.5 m ($F/5$) telescope focal plane has substantial curvature and they use TDI (time-delay and integration) drift-scanning for the survey, they invented a novel “ball-and-cone socket” mount which allowed for a precise adjustment for the tilt, rotation, and piston of each CCD down to the level of a few tens of μm .

In the late 1990s, three-sided buttable $2\text{K} \times 4\text{K}$ CCDs with 15 μm pixels became available from several manufacturers including the MIT/Lincoln Laboratory, SITe, and EEV, and were used in various astronomical cameras in which closely packed mosaic configurations were crucially requested. One of them is the Suprime-Cam, built for the 8.2 m Subaru Telescope's $F/1.8$ prime focus (Miyazaki et al. 2002). Because of the fast beam, the requirements on the co-planarity of the mosaic arrays were demanding. By inserting thin metal foils between the CCD package and a buffer block which has position-alignment pins for the cold plate, they realized 20 μm co-planarity over the 5×2 mosaic ($\sim 15 \text{ cm} \times 12 \text{ cm}$). One corner device, however, was 30 μm out of planarity because of the bumpy intrinsic surface profile of the CCD itself. MegaCam (Boulade et al. 2003) for the 3.6 m Canada-France-Hawaii Telescope (CFHT) $F/4$ prime focus adopted $40 \times 2\text{K} \times 4.5\text{K}$ (13.5 μm pixels) EEV CCDs to realize a $1^\circ 4$ diameter field of view, where a similar level of the co-planarity is achieved (32 μm).

Suprime-Cam has been one of the foremost observing facilities for surveying the distant universe. However, surveys to probe cosmic acceleration with wide-field imaging require unrealistically large observing times given Suprime-Cam's field of view of 0.25 deg^2 . We, therefore, decided to build a camera with an even larger FOV to make such surveys possible, while maintaining an image quality as high as that of Suprime-Cam. We call this new camera the “Hyper Suprime-Cam”. At almost the same time, a group led by Fermi lab proposed the Dark Energy Camera (DECam) for Blanco 4 m telescope whose field of view is $2^\circ 2$ in diameter (Flaugher et al. 2015). DECam is designed and built over the same time period as Hyper Suprime-Cam.

In order to realize the new camera project, an international team of astronomers and engineers has been formed

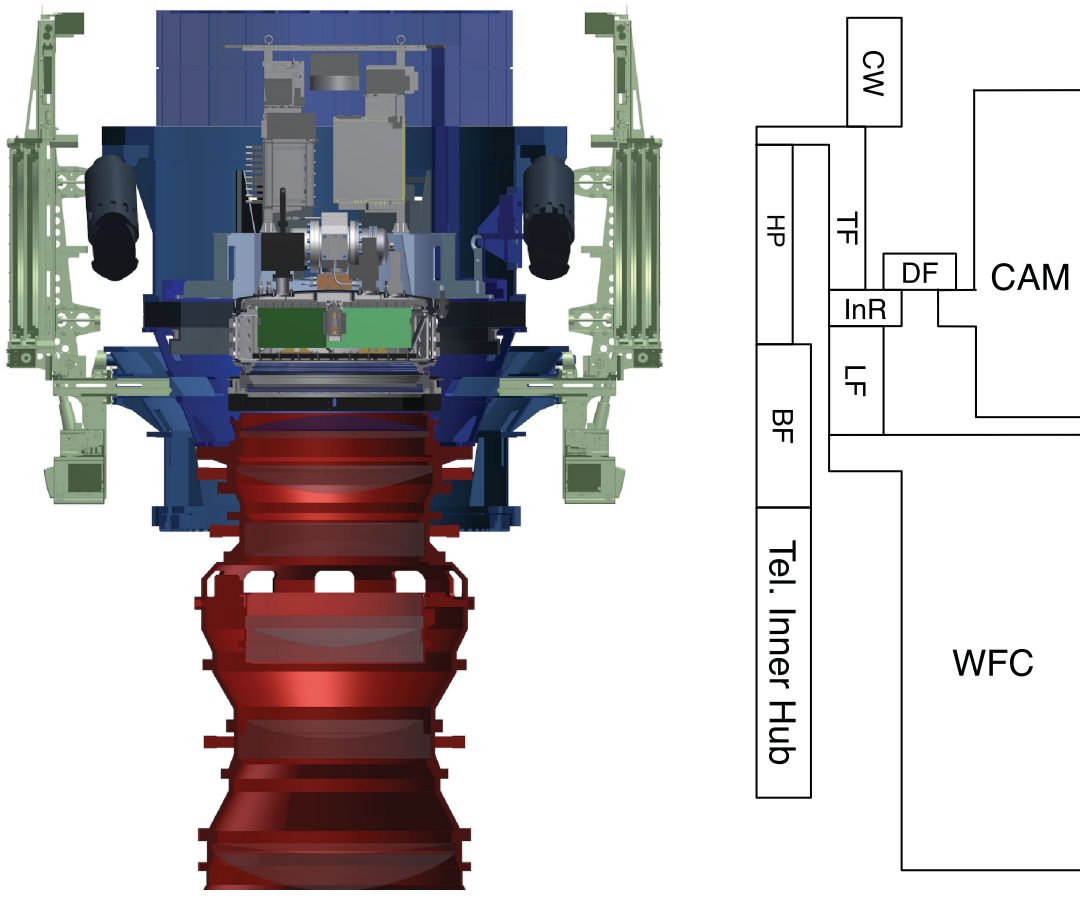


Fig. 1. Cross-sectional view of Hyper Suprime-Cam. The configuration of the system units is schematically shown on the right. The filter exchanger unit (FEU) is not shown in the diagram. The abbreviations are defined in table 1.

from various institutes, including the National Astronomical Observatory of Japan, the Kavli IPMU University of Tokyo, the High Energy Accelerator Research Organization (KEK), Nagoya University, Tohoku University, Academia Sinica Taiwan, and Princeton University, USA. Our industrial partners include Mitsubishi Electric, Hamamatsu Photonics, and Canon.

We submitted an observing proposal to a category of the Subaru Strategic Program (SSP) with more than 200 co-investigators from Japan, Taiwan, and the US aiming to carry out a legacy optical imaging survey using the Hyper Suprime-Cam (HSC). The SSP survey consists of three tiers: Wide, Deep, and Ultra-Deep. SSP-Wide is designed to be a competitive cosmological survey in which a nearly 10 times larger survey field is covered with one magnitude deeper imaging compared with the existing Canada–France–Hawaii Legacy Survey (CFHLS). SSP-Deep and SSP-Ultra-Deep uniquely combine narrow-band imaging with broad-band imaging to explore frontiers of science in high-redshift objects and galaxy evolution. Three hundred nights were awarded to the proposal; the survey started on 2014 March, and will continue for about six years.

In this paper, we describe the camera system with particular focus on how to realize seeing-limited imaging: the system design and the estimate of the image quality (section 2), the design of the wide-field corrector (section 3), and the focal plane array (section 4). We present the results of images taken with the commissioning observations (section 6). A series of papers is planned that describe each of the camera’s components in more detail; the cryogenic dewar by Komiyama (2017), filters and the camera calibration system by Y. Kawanomoto et al. (in preparation), CCD readout electronics by H. Nakaya et al. (in preparation), and CCD evaluation and characterization by Y. Kamata et al. (in preparation). The survey design of the SSP program is described in Aihara et al. (2017a).

2 System design

2.1 Layout of HSC system components

First, we show the system components of the HSC and their layout. The cross-sectional view of the HSC is shown in figure 1, and the perspective view in figure 2. There are

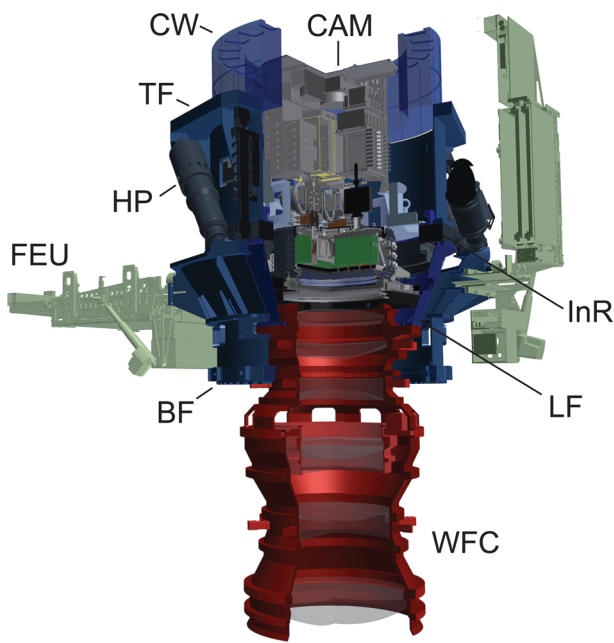


Fig. 2. Diagrammatic perspective view of Hyper Suprime-Cam. The abbreviations are defined in table 1.

three major system units, the Camera (CAM), the wide-field corrector (WFC), and the main chassis body that holds both CAM and WFC. We call that POPT2 (the chassis for Suprime-Cam is called POPT). It is designed and built by Mitsubishi Electric Corporation (Ezaki & Endo 2014). Table 1 shows the list of the HSC system units and their sub-systems.

This system configuration and arrangement are basically equivalent to those of Suprime-Cam. POPT2 has a hexapod mechanism that collimates the CAM and WFC systems with respect to the optical axis of the primary mirror. The mechanical connection path between the telescope and CAM is as follows: telescope flange—base frame—hexapod—top frame—instrument rotator—CAM.

The instrument rotator is hung by the top frame. Because the housing of the instrument rotator is stiff enough, it can be used as a base for the dewar frame and the lens frame, on which the CAM and WFC are mounted, respectively. It would be ideal if we attached one end of the hexapod as close as possible to the center of gravity (CoG) of the system. This is especially true for HSC, where the CoG is very low due to the large, heavy WFC. In the initial conceptual studies of the HSC, we explored the possibility of placing the hexapod inside the inner hub of the telescope's top ring. To keep sufficient space for the WFC, we had to use a much wider inner hub, which would have been quite costly and impractical. Therefore, we returned to the original (Suprime-Cam) configuration as described. Because the prolonged top frame holds the entire weight of the WFC

Table 1. HSC system units.

Abbreviation	Description
Wide-field corrector (WFC)	
Lens	Corrector lens system.
Barrel	A structure to hold the Lens system.
ADC	A pair of glass elements in the Lens that can be laterally shifted and act as the Atmospheric Dispersion Corrector.
POPT2	
BF	The Base Frame is the foundation structure of the entire HSC system and connects the telescope inner hub and Hexa-Pod.
HP	The Hexa-Pod controls the attitude and position of the HSC. HP is located between the BF and the top frame. Each actuator in the HP is similar to those developed for POPT, i.e., the prime focus unit for Suprime-Cam.
TF	The Top Frame hangs the instrument rotator, CAM, and WFC from the top of the POPT2.
InR	The Instrument Rotator rotates CAM in order to compensate for the field rotation.
DF	The Dewar Frame supports CAM.
LF	The Lens Frame holds WFC to the fixed side of the instrument rotator.
CW	The Cable Wrapper wraps cables and hoses in order to remove the slack caused by the rotation of the InR.
Camera (CAM)	
Dewar	The cryogenic Dewar holds detectors and keeps their temperature down to -100°C .
FP	The mosaic of 116 $2\text{ K} \times 4\text{ K}$ CCDs which paves the Focal Plane.
FEU	Filter Exchange Unit.
Filter	Broad-band ($\sim 100\text{ nm}$) and narrow-band ($\sim 10\text{ nm}$) pass filter set.
Shutter	Focal plane shutter consisting of two sets of screens.
SH	Shack–Hartmann wave-front sensor mounted inside a filter frame.

and CAM in this configuration, we gave special attention to the deformation of the top frame (in particular, to the hysteresis that could not be corrected by hexapod).

Only the CAM is rotated by the instrument rotator, allowing the CAM to follow the image rotation of the alt-azimuth telescope. The WFC is fixed. Because there is not sufficient space for the filters inside the POPT2, we need to have an external filter holder and a filter exchange mechanism (FEU). We have two sets of FEUs, and each holds three filters. The base frame and the lens frame have slits for the filter insertion.

Table 2. Image error component estimates of the HSC in the *i* band (elevation >30°).

FWHM ["]	Error component	Δ FWHM ["]	Related subsystem	Δ FWHM ["]
0.336	Diffraction	0.036		
	Primary mirror	0.150		
	WFC aberration	0.138		
	Tracking	0.139	Telescope mount drive	0.130
			Inst. rotator drive	0.048
	Collimation	0.110	WFC setting error	0.002
			FP tilt: Flexure	0.014
			Manufacturing	0.047
	CCD charge diffusion	0.184	FP defocus: Manufacturing	0.034
	Filter parallelism	0.050	FP flatness: CCDs	0.092
	Window parallelism	0.050		

2.2 Image error component estimates

In this subsection, we estimate the expected image quality of HSC by adding the various error components in quadrature. Here we simply include the worst-case value for each component, which makes our estimate rather conservative. Table 2 summarizes the results of estimates which are described in the following sections. The estimated instrument point spread function (PSF) is 0''.336 [full width at half (FWHM)] in the worst case.

Before we discuss the image error, we describe a coordinate system that is fixed on the telescope tube framework. We adopt the normal left-hand coordinate system, the z -axis of which points to the pointing direction of the telescope. The x -axis is chosen in parallel with the direction of the elevation axis and the telescope elevation declines when it rotates in the $+θ_x$ direction. Therefore, the y -axis points to the “rear” side of the telescope. The decenter and the tilt of the optical component are represented as $(Δx, Δy)$ and $(Δθ_x, Δθ_y)$, respectively.

2.2.1 Diffraction limit, primary mirror, and WFC

The diffraction is approximated by $1.22λ/D$ [rad] where $λ = 0.775\text{ μm}$ and $D = 8.2\text{ m}$. The conversion factor from this 2D rms number to FWHM is 1.67.

The primary mirror (M1) of Subaru is supported by 261 actuators. The residual surface error measured by the Shack–Hartmann (SH) wavefront sensor is reported to be typically 300 nm (rms), which is equivalent to 0''.15 (FWHM) (Iye et al. 2004).

For the WFC, we put the image error of 0''.14 (FWHM) [Elevation (EL) = 30° and in the HSC-*i* band] which is estimated from the wavefront error measurement (section 3). It includes both the design error and the manufacturing error.

2.2.2 Tracking error

The instability of the telescope tracking causes image degradation. This tracking error is a superposition of the following errors: the telescope mount drive error, and the drive error of the rotator motor.

An open-loop tracking error is reported to be 0''.2 (rms) for 10 minutes, and a closed-loop tracking using a auto-guider is better than $~0''.1$ (rms) (Iye et al. 2004). Here we assume 0''.08 (rms) for the guided tracking error, which corresponds to 0''.13 (FWHM).

Ezaki and Endo (2014) reported that the angular drive error of the InR motor, $θ_R$, is 2''.2 (rms). The image elongation $Δl$ at the 480 mm diameter focal plane edge is 2.6 $μ\text{m}$ (rms), which corresponds to an angular scale of 0''.048 (FWHM). The sub-total of the two components of the tracking error added in quadrature is therefore 0''.139.

2.2.3 Collimation error

On the Subaru telescope system, the collimation of the secondary mirror (M2) with respect to M1 is realized by a hexapod of M2 based on the elevation-dependent control parameters which are generated through the mirror analysis using the SH wavefront sensor (Iye et al. 2004). The decenter of M2, which mainly causes a comatic aberration, is thus one of the mirror analysis parameters. The actual operation of the telescope is based on the static table of the control parameters, and no real-time wavefront measurement is made. In the case of the prime focus operation, the control scheme is the same as that of M2 mentioned above. HSC has a SH sensor mounted in one of the filter frames (Morokuma et al. 2008) and it is loaded when the mirror analysis is carried out.

2.2.4 WFC setting error

The basic collimation of the WFC with respect to M1 is thus realized by the hexapod based on past mirror-analysis

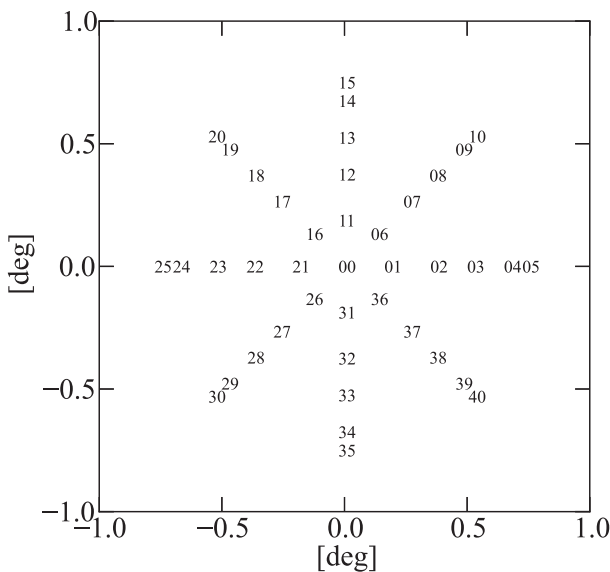


Fig. 3. Forty-one field positions considered in the sensitivity analysis. One position is at the center of the field (on-axis). On the positive side of the x -axis, we have five off-axis positions at $x = 0^\circ 1875, 0^\circ 375, 0^\circ 525, 0^\circ 675$, and $0^\circ 75$. These are subsequently rotated by 45° seven times to define 40 off-axis field positions.

parameters. However, errors exist in the setting of the WFC, caused by the hexapod drive error.

We assess the impacts of these setting errors by adopting results of a simple sensitivity analysis described here. Using the optics model of the telescope and WFC, we evaluate the deterioration when we add a small decenter and tilt on the designed fiducial position parameters. We used the WFC optics model with an elevation of 30° because it has a larger aberration than that of zenith (section 3). We chose the central wavelength of the HSC-*i* band (760 nm) for this analysis. We determined the worst deterioration in the PSF for 41 points over the field (figure 3). The deterioration, expressed as an increase of FWHM, is approximated by a linear function of the input perturbation, and the sensitivity coefficients are obtained for the decenter and the tilt. Figure 4 shows how we determined the coefficient for the focal plane tilt as an example.

Table 3 summarizes the sensitivity coefficients, allowing the conversion between a given perturbation and the deterioration of the PSF.

The drive error of the hexapod of the HSC is reported to be a few μm (Ezaki & Endo 2014). We assume it to be $3 \mu\text{m}$ here for each component, $\Delta x = \Delta y = \Delta z = 3 \mu\text{m}$. We assign $0''.6$ for $\Delta\theta_x$ and $\Delta\theta_y$ ($= 3 \mu\text{m}/1000\text{mm}$ scale). All of the components (Δx , Δy , Δz , $\Delta\theta_x$, and $\Delta\theta_y$) are added together in quadrature, yielding $\Delta\text{FWHM} = 0''.002$.

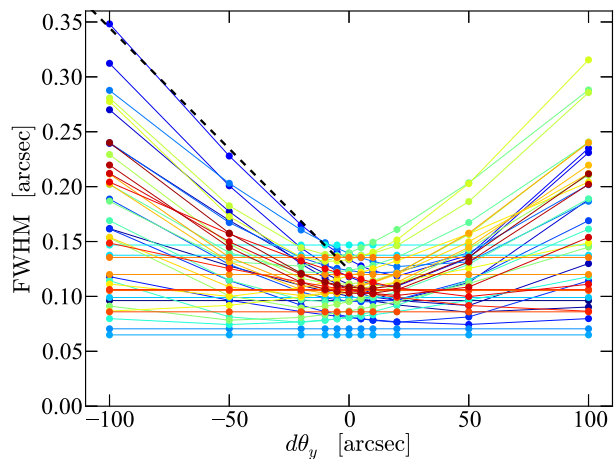


Fig. 4. Example plot generated for the sensitivity analysis. Image size is evaluated by rms, which is converted to FWHM by multiplying by a factor of 1.67. The size is shown as a function of the input focal plane tilt around the y -axis. All the data calculated at the 41 field positions are superimposed. The sensitivity depends on the field position. We linearly fit the data on the positive and the negative sides of the input $d\theta_y$ separately, and searched for a field whose slope is hardest. The thick dashed line shows the best fit for the identified field, and the slope is adopted for the sensitivity of the focal plane's tilt around the y -axis.

Table 3. Result of the sensitivity analysis in the *i* band ($EL = 30^\circ$).*

Sub-system	$\Delta \text{FWHM}^\dagger$	
	[arcsec mm $^{-1}$]	[arcsec deg $^{-1}$]
WFC	Δx	0.30
	Δy	0.33
	Δz	4.34
	$\Delta\theta_x$	5.39
	$\Delta\theta_y$	5.02
	Δz^*	0.34 (3.02)
FP	$\Delta\theta_x$	8.43
	$\Delta\theta_y$	7.93

*The coefficient for Δz of FP is calculated by allowing for the focus readjustment.

†A value in parentheses shows the coefficient when no focus readjustment is made.

Focal plane tilt

There are other independent sets of collimation errors, which are caused by the misalignment between the WFC and the focal plane. The misalignment has two cases: tilt and defocus.

As one origin of focal plane tilt with respect to the WFC, we first consider the flexure due to the change of the elevation of the telescope. Here, we assume that WFC is always collimated as designed with respect to the M1 optical axis by the hexapod while the elevation changes. The error of this collimation has been already discussed in the previous sub-subsections.

As shown in figure 1, the dewar is mechanically connected with the WFC via the lens frame, the instrument rotator, and the dewar frame. The focal plane is supported by the truss structure inside the dewar (Komiyama 2017). Finite element method (FEM) analysis suggests that the deformation of the lens frame causes a focal plane tilt of $\Delta\theta_x \sim 6''$ when we change the elevation from 90° to 30° . No significant deformation is observed in the instrument rotator and the dewar frame. The flexure inside the dewar is less than $1''$ and is also negligible. The lower part, labeled “FP” in table 3, shows the sensitivity coefficients calculated for the focal plane tilt with respect to the WFC. Using this table, the error components related to the flexure amounts to $\Delta\text{FWHM} = 0''.014$, by using $\Delta\theta_x = 6''$.

Manufacturing errors of each mechanical unit are another source of the focal plane tilt. Although they can be measured and corrected in principle, we include them in the error estimate. The standard tolerance of the machining of meter scale components is $50\,\mu\text{m}$ and the same is true for the specification of parallelism of the lens frame, the instrument rotator, and the dewar frame. This could cause a maximum tilt of $10''$ for 1 m, which is roughly the diameter of those three components. So we consider this tilt as the manufacturing error of the two frames and the rotator. The tilt of the focal plane with respect to the dewar frame is reported to be $7.2\,\mu\text{m}$ (Komiyama 2017). Here we adopt a $10''$ tilt as well for simplicity. In total, the image deterioration caused by these four manufacturing errors through the focal plane tilt amounts to $\Delta\text{FWHM} = 10'' \times \sqrt{4} \times 8.43/3600 = 0''.047$, where $\sqrt{4}$ reflects the fact that we are combining the four components in quadrature.

Focal plane defocus

The setting error of the distance, Δz , between the WFC and the focal plane causes defocus. We again consider the machining error of $\Delta z = 50\,\mu\text{m}$ for all four components that connect the WFC and the focal plane. These setting errors can be relieved somewhat by readjusting the focus position using the hexapod, but a residual will still remain because the distance between M1 and the WFC departs from the designed value. The deterioration coefficient for FP’s Δz shift is calculated, and it is listed in the lower part of table 3. (The value in the parentheses is the coefficient where no focus readjustment is considered.) We add the four components in quadrature yielding $\Delta\text{FWHM} = 0''.34 \times 50/1000 \times \sqrt{4} = 0''.034$.

Focal plane flatness

We install a mosaic of $104\,2\,\text{K} \times 4\,\text{K}$ CCDs for the science imaging on the cold plate inside the dewar. The CCD coplanarity depends both on the surface flatness of the cold plate and on the CCD flatness. The surface manufacturing

tolerance and the global warp of the cold plate are considered, and they are estimated to be $15\,\mu\text{m}$ and $10\,\mu\text{m}$, which correspond to the error of $0''.045$ and $0''.030$, respectively.

For each CCD, we require that the light-incident surface should be located within the two fiducial planes which are parallel to the bottom surface of the CCD. The distance between the planes is $35\,\mu\text{m}$. This global flatness is required to guarantee the coplanarity of the entire mosaic. The peak-to-valley value is translated into rms by dividing by $\sqrt{2}$, which is then converted to $\Delta\text{FWHM} = 0''.074$. For both cases, we use the Δz coefficient, in which we do not consider the focus readjustment because the local focus error cannot be eliminated by the focusing. We take the Root Sum Squared (RSS) of these errors, yielding $0''.092$ for the focal plane flatness.

The total RSS error for the collimation, including all effects described in this sub-subsection 2.2.4, amounts to $\Delta\text{FWHM} = 0''.110$.

2.3 Other error components

Charge diffusion in the thick, fully depleted CCDs is not negligible, and smears the images (section 4). The measured charge diffusion in the $200\,\mu\text{m}$ thick CCD is $\sigma_D \simeq 7\,\mu\text{m}$ for the $450\,\text{nm}$ lights, which corresponds to an angular scale of $0''.184$ in FWHM.

There are two other optical components in addition to the WFC: the filter and the dewar window. We specify a parallelism requirement of $40''$ for each of them which results in $\Delta\text{FWHM} = 0''.05$ for each.

3 Wide-field corrector

3.1 Requirement

Table 4 summarizes the requirements for the WFC regarding the image size in the standard broad-band filters. The image error estimate in the previous section was based on rms error (and then converted to FWHM) because the rms is the appropriate statistic for describing mechanical errors. In the optical ray-tracing, the rms scatter tends to become larger even if a tenuous outskirt of the spot exists. The outskirt, however, cannot be observed in the actual observation where we have photon shot noise from the sky. Therefore, the rms may overestimate the image size in a practical sense. Instead, we adopt the 80% encircled energy diameter, D_{80} , for the optics specification. For a Gaussian profile, the conversion is given by $D_{80} = 1.52\,\text{FWHM}$. We require $D_{80} = 0''.3$ for the r , i , and z bands but loosen the specification for the g ($0''.5$) and y ($0''.4$) bands where lensing analyses are not usually carried out. Because the observing log of Suprime-Cam for nearly 10 years showed that 95%

of the observations are done with an angle of elevation (*EL*) between 30° and 85° , we set the lower limit of the *EL* at 30° in the specification.

3.2 Optical design

A Wynne triplet (figure 5a) is the basis of the WFC for R-C telescopes (Wynne 1968). At least three lenses (8 degrees

of freedom) were necessary to define the focal length and the focus position, and to compensate for spherical aberration, coma, astigmatism, field curvature, and the chromatic aberration of magnification. The second-order chromatic aberration is suppressed well by adopting the same glass (UBK7) for all lenses, but this has a drawback of limited wavelength coverage.

The specification of the WFC for the Subaru prime focus is more demanding in image size and wavelength coverage. As briefly described in section 1, Takeshi (2000) designed a WFC that realized $D_{80} < 0''.15$ even at the edge of the $30'$ diameter field of view by adopting aspheric figures and ultralow dispersion glass (FPL51 from Ohara). It also has a novel lateral shift atmospheric dispersion compensator (ADC), where a pair of lenses are shifted vertically off-axis, acting as a virtual prism with a variable vertex angle. In addition, these lenses work as a doublet (achromatizing lens) and function as the parts of an aberration corrector. This makes the corrector more compact than a conventional ADC made of a pair of rotational prisms does. Another advantage of the ADC design is that the images do not shift. This WFC design is used for Suprime-Cam.

HSC's WFC was also originally designed by K. Takeshi (Komiyama et al. 2006). In the initial phase of the conceptual studies, our target field diameter was 2° . The design realized an image quality $D_{80} < 0''.26$ over the field at wavelengths between 600 and 1100 nm. All the glasses

Table 4. Designed performance in each pass-band as quantified difference of D_{80} .*

Filter	Spec. ["]	<i>EL</i> = 90° ["]		<i>EL</i> = 30° ["]	
		Design	Est.	Design	Est.
(u)	—	(0.428)	—	(0.495)	—
<i>g</i>	<0.5	0.163	0.199	0.196	0.234
<i>r</i>	<0.3	0.150	0.197	0.187	0.232
<i>i</i>	<0.3	0.146	0.200	0.191	0.233
<i>z</i>	<0.3	0.151	0.206	0.186	0.214
<i>y</i>	<0.4	0.199	0.210	0.216	0.228

*Image size specifications for WFC in D_{80} (80% encircled energy diameter) and the designed performance (worst case) at elevations of 90° and 30° . The employed wavelengths in each pass-band (equal weight) are $g = (420, 470, 530)$, $r = (570, 620, 670)$, $i = (710, 760, 820)$, $z = (870, 910, 960)$, and $y = (970, 1020, 1070)$ [nm]. The *u* band (350, 370, 390) [nm] performance is not specified, but the designed values are shown for reference. The final image sizes are estimated from the actual performance verification test measurements (see text in subsection 3.4).

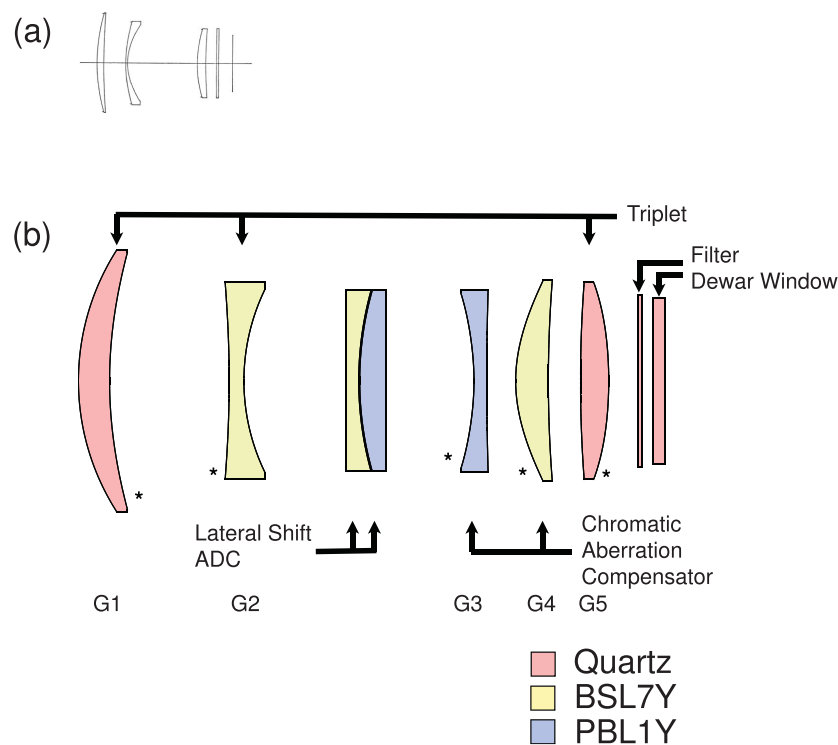


Fig. 5. (a) Wynne Triplet for the Kitt Peak 4 m telescope. (b) Wide-field corrector designed and built for Hyper Suprime-Cam. “**” denotes that the surface is aspheric.

Table 5. Requirements for the glass blank.

Striae	No visible striae
Birefringence	$\leq 5 \text{ nm cm}^{-1}$
Refractive index uniformity (homogeneity)	$\pm 5 \times 10^{-6}$
Abbe number uniformity	$\pm 0.5\%$

Table 6. General optical data.

Focal length	18320 mm
Image scale	$0.888 \text{ mm arcsec}^{-1}$
Image size ($1^\circ.5$)	495 mm (diameter)

were fused silica glass, except one optical glass (S-BSL7). By adopting 1.2 m diameter glass for the first lens, the vignetting is smaller than 20% at the field edge. However, a WFC with a 1.2 m diameter turned out to be too large to accommodate without significantly modifying the telescope structure. Thus we reduced the field of view to $1^\circ.5$.

The WFC optics layout that meets all the specifications is shown in figure 5b. There were several variants through the development phase but the final design configuration turned out to be the same as that of Suprime-Cam's WFC. It is composed of a basic Wynne triplet (G1, G2, G5) and the lateral shift ADC followed by a pair of lenses (G3, G4) that compensates for chromatic aberration introduced by the ADC (Matsuda et al. 2010). The last two flat elements are a 15 mm thick filter and a 37 mm thick dewar window.

The design adopts aspheric surfaces on multiple elements; the maximum deviation from the sphericity is 5 mm. The asterisks on figure 5b show the location of the aspheric surface. Note that some of the surfaces use a convex-aspheric surface which is usually avoided in camera design because of the complexity of the measurement setup. Canon has invented a high-precision (5 nm rms) contact-type free-form measurement machine, called A-ruler (Negishi 2001), that is used for the metrological characterization of the large aspheric surface.

The lenses are made of synthetic silica (quartz), BSL7Y, and PBL1Y. The glass selection was made based on the availability of the large (>60 cm diameter) glass blanks needed. Table 5 shows requirements on all the glasses that we adopted except G1 (the first quartz lens) where we specify the higher homogeneity of 3 ppm. We procured the silica from Corning and optical glasses from Ohara. The G1 lens is 82 cm in diameter and the size constraint comes from the diameter of the inner hub of the top ring of the Subaru telescope.

General optical data for the WFC design are shown in table 6. The image size is larger than the paraxial image size (about 480 mm) because of the distortion (+3.2%).

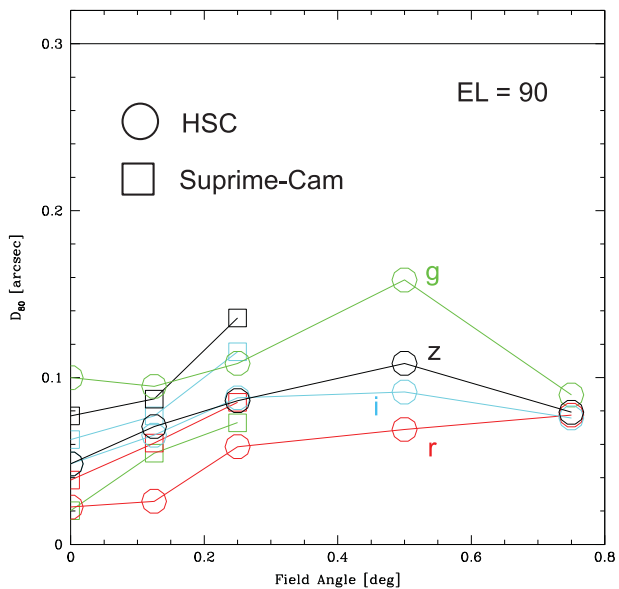


Fig. 6. Designed performances of the wide-field corrector (Suprime-Cam: square; HSC: circle) in each filter band as a function of field angle from the center.

3.2.1 Designed performance

In table 4 we summarized the designed performance in each pass-band as quantified difference of D_{80} . From the ray-tracing we examined the images of 41 sample field positions (figure 3), the worst case is presented in table 4. The designed performance satisfies the specification with large margins. This allows for the manufacturing (figuring and assembly) errors and environmental change. Figure 6 shows the comparison of the designed performance of Suprime-Cam (square) and that of HSC (circle) at zenith. HSC's designed performance is almost equivalent to that of Suprime-Cam. Note that the largest aberration does not always occur at the edge of the field of view. This is because the vignetting at the field edge (see figure 9) eliminates rays with large heights which tend to have larger optical path differences. One also notes that an HSC's WFC design gives better performance at redder bands (r, i), which is in contrast to the Suprime-Cam's design where the g band had the priority.

The gray-scale images in the left-hand side of figure 7 show the PSF in the i band calculated using ray-tracing. The expected PSFs convolved with $0''.4$ (FWHM) Gaussian seeing are shown in the right-hand. When we compare the in-focus and out-of-focus images, we see a 90° rotation of the image smear direction, except for the outermost field angle of $0^\circ.75$ where the vignetting is significant. The 90° rotation is due to the astigmatism inherent in the optics design. Figure 8 shows the PSF when the elevation is set at 30° . The atmospheric dispersion is considered in the input rays and the ADC is laterally engaged so that the dispersion

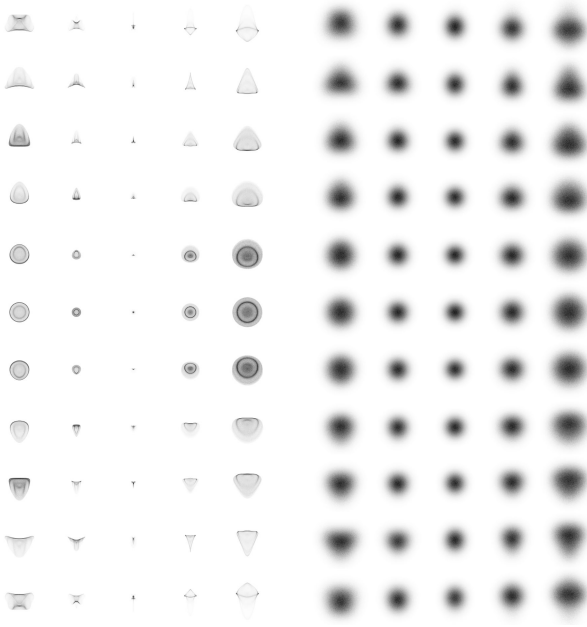


Fig. 7. Gray-scale images of the PSF obtained from the optical design in the *i* band (left). From the left-hand column to the right-hand, the focus position is changed from -100 to $+100\ \mu\text{m}$ in steps of $50\ \mu\text{m}$. Each row represents the field angle in the *y*-direction from $-0^{\circ}75$ (bottom) to $+0^{\circ}75$ (top) in steps of $0^{\circ}15$. The PSF is convolved with $0^{\circ}4$ (FWHM) Gaussian seeing (right). The telescope elevation is set at 90° .

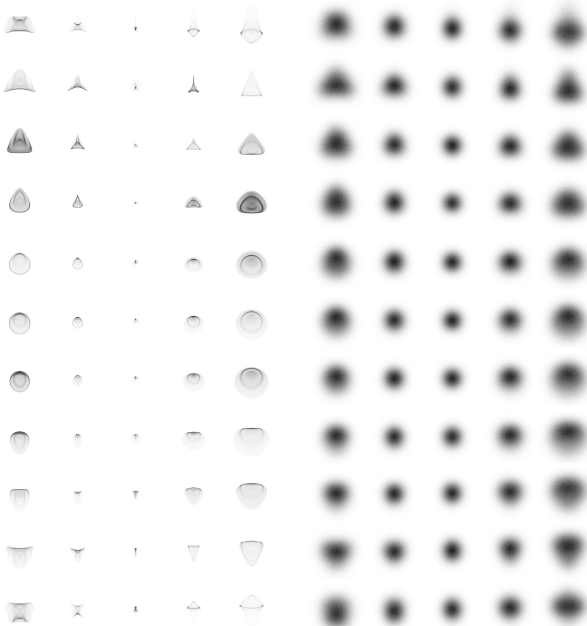


Fig. 8. Same as figure 7 for the elevation of 30° .

is minimized. We observe the asymmetry of the PSF across the field of view.

The G1 lens blocks a part of the incoming off-axis beam which results in vignetting: the radial profile of this is shown in figure 9. The maximum vignetting occurring at the edge of the field is 25.6% ($\theta = 0^{\circ}75$). Although it decreases

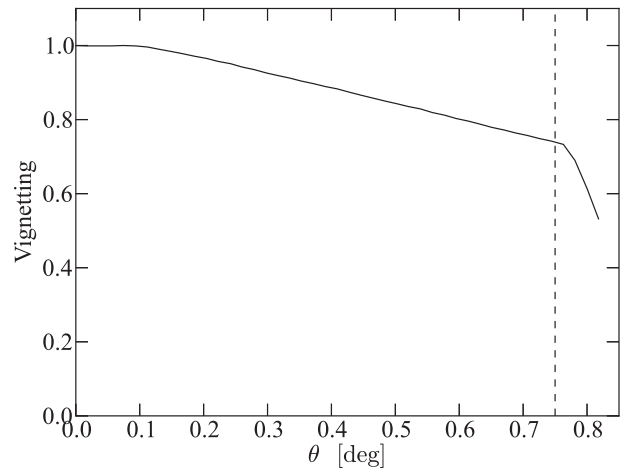


Fig. 9. Radial profile of the vignetting of WFC. Dashed line shows the edge of the field of view ($0^{\circ}75$).

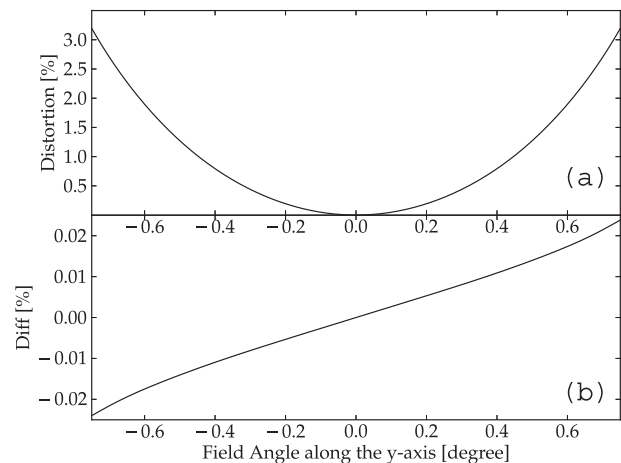


Fig. 10. (a) Distortion of WFC at $760\ \text{nm}$ with $EL = 90^{\circ}$. (b) Distortion in the case of $EL = 30^{\circ}$ relative to $EL = 90^{\circ}$.

rapidly, we still have lights at $\theta > 0^{\circ}75$. This area is used for the focus CCDs (subsection 3.6).

The distortion at $\lambda = 760\ \text{nm}$ (the center of the *i*-band filter) and $EL = 90^{\circ}$ is shown in figure 10a. Fitting it with a fourth-order polynomial yields

$$f(y) = 1.77y^4 + 4.63y^2, \quad (1)$$

where y is a field angle in degree and $f(y)$ is shown in percentage. There is a slight dependence on the wavelength, and at the field edge it varies from 3.181% to 3.177% from the *g* band to the *y* band.

Because of the differential effect, the distortion stretches the image radially and the aspect ratio of the stretched elliptical is represented as $r = b/a = (1/100)df(y)/dy$. The azimuthally averaged image size is presented as $d_0\sqrt{1+r}$, where d_0 is the original size before the stretch. At the field edge we have a 6% image stretch. Note that this simply

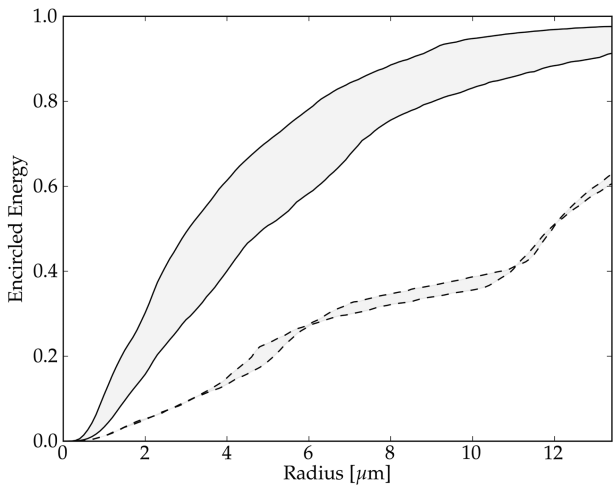


Fig. 11. Growth curve of the encircled energy as a function of radius in the r band with $EL = 30^\circ$ at Mauna Kea. The end point of the horizontal axis ($13.4 \mu\text{m}$) corresponds to the specification $D_{80} = 0''.3$. Solid lines show the case when the ADC was properly engaged, whereas dashed lines are the case when the ADC was not engaged (fixed at the center). Two lines in each case correspond to the field angle of $0^\circ675$ and $0^\circ375$, where the smallest and the largest D_{80} is realized, respectively.

reflects an increase of the plate scale with approaching the field edge and is not an image smear.

3.2.2 Atmospheric dispersion corrector (ADC)

The lateral shift ADC consists of two glass elements, the indices of which should ideally be the same for the central wavelength in the ideal case. The first and third surfaces are made flat and the second has a curvature. Therefore, this ADC is a plane-parallel element for the central wavelength ray and does not refract it. For rays at other wavelengths, it works as a doublet and gives a refraction with a sign that is positive for wavelengths longer than the central wavelength and negative for shorter wavelengths. By shifting the doublet laterally, we are able to control the refraction angle to cancel the atmospheric dispersion. The effect of the ADC is quite significant, as shown in figure 11. Without the ADC, D_{80} is significantly larger than $0''.3$ for a broad-band filter.

Because the central wavelength depends on the filter, the ray of the central wavelength suffers from refraction in general. Therefore, if the ADC is shifted and the refraction angle is changed, the image is focused at a deflected position, which looks like a distortion. In this way, we have an elevation-dependent distortion. The dependence can be minimized by matching the refractive indices of the two glass elements. In the case of Suprime-Cam, S-BSM14 and S-TIM5, for which $\Delta n = 0.0017$, are used. Because of the limited selection of large glass blanks used for the HSC WFC, the only possible combination was a combination of BSL7Y and PBL1Y, which results in the larger index difference of 0.0327. The difference of the distortion between the EL of 30° and that of 90° is shown in

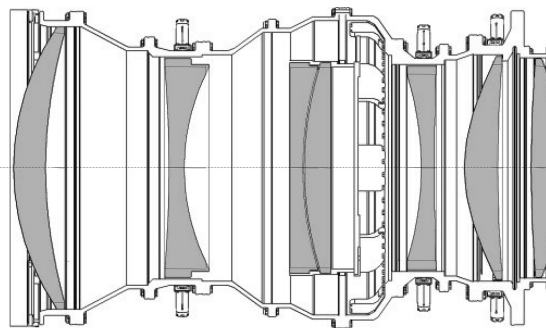


Fig. 12. Lens barrel assembly of WFC. Circular frames that hold each lens are connected with intermediate circular frames. S-Lec (see text) centering mechanism are attached on G2, G3, and G4.

figure 10b: it reaches up to 0.02% at the field edge ($\sim 0''.54$). This effect has to be taken into account during the data processing. The axisymmetric distortion model does not work.

3.3 Lens barrel assembly

Each lens is put into a circular frame which is made of a ceramic, cordierite, the thermal index of which matches well with the silica. An inner annular plate is attached with springs located in a circle, which settles the lens with an appropriate pressure. Each lens frame is stacked with an intermediate frame for spacing (figure 12) on a precision air-bearing rotation stage, the decenter of which is controlled at the μm level. The lens is precisely aligned with respect to the outer shape of the frame and is then used as the reference during the stacking phase. The tolerance allowed for decenter and tilt is $\pm(30\text{--}50)\mu\text{m}$ and $\pm 15''$, respectively (Imoto et al. 2014).

Cordierite is the only material that we could adopt given our tight weight constraints. However, the cordierite is very brittle. Thus we must exercise great caution when handling the WFC. The cordierite has a coefficient of thermal expansion (CTE) that matches well with that of quartz. However, the CTE of the optical glass adopted in this case is significantly larger, which may cause the lens to decenter with respect to the cordierite frame after experiencing a temperature change. We installed a set of radial invar rods to constrain the decenter. The rods are mounted with intentionally high CTE metal (zinc alloy) to keep the appropriate surface pressure between the rods and the lens when the temperature changes (Subaru Lens Centering mechanism, S-Lec).

We simulated the image deterioration caused by the deformation of the lens and its barrel due to its own weight. The Lens Frame that holds the barrel is also included in the simulation and the enforced displacement, estimated from an independent FEM analysis, is applied to the boundary with the rest of the camera system. At $EL = 30^\circ$ in the i band the D_{80} is roughly 20% larger. This is acceptable,

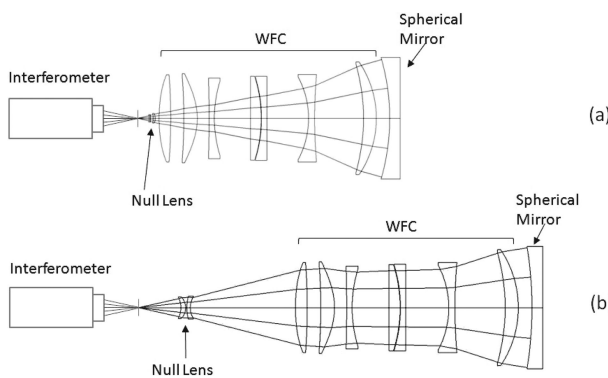


Fig. 13. Performance verification setup of WFC.

considering the large margin in the designed performance (sub-subsection 3.2.1).

3.4 Performance verification test of WFC

We tested the WFC performance in two steps. First we measured the image at the field center. An interferometer (633 nm) provided a light beam into the WFC from the backside. We set the focus of the spherical light from the interferometer at the focus of WFC. A concave mirror reflects the light beam back to the WFC and we observe the fringe pattern with the returning light beam, as schematically shown in figure 13a. The light beam from the interferometer is adjusted to be focused at the WFC focus position. The concave mirror surface is designed normal to the incident light so that we have refocusing of the beam at the same WFC focus position. A null lens is designed so as to mimic the aberration that the hyperboloid M1 generates and is put into the beam. The resulting fringe pattern also gives a rough estimate of what commits any errors. For example, the decenter of any lens would cause a comatic aberration, while a rotationally symmetric figuring error would cause a spherical aberration. The rms wavefront error observed on the finally assembled WFC was 77.24 nm.

We would like to estimate the impact of the assembly error on the image quality. The purpose of the WFC is to cancel the aberrations generated by M1. If the WFC is perfectly designed and manufactured, no fringes would be observed. But this is not the case. The WFC design itself causes a residual but known wavefront error, Δz_R , and the manufacturing process causes another wavefront error, Δz_M . The observed wavefront error, Δz_O , is the sum of the two:

$$\Delta z_O = \Delta z_R + \Delta z_M. \quad (2)$$

In order to estimate the final image quality, we paste the 2D wavefront error of the manufacturing error of $\Delta z_O - \Delta z_R$ on the design pupil (M1) and carry out the ray-trace. By

subtracting Δz_R , we avoid double-counting the aberration inherent in the design.

As shown in figure 13a, the on-axis test is only sensitive to the error of the forward lens elements (i.e., those closer to M1). Off-axis performance verification is necessary for checking the setting of the rearward lenses but it is harder to implement because it requires a larger optics setup. Therefore, instead of an off-axis test, we set the focus of the spherical light from the interferometer at the position where the outermost rays of the WFC cross the optic axis (figure 13b). Thus, the beam passes through the entire lenses. When we estimate the image quality at an off-axis field angle, we add the difference of the 2D wavefront error obtained this way to the last surface of WFC. Table 4 shows the crudely estimated worst-case D_{80} . We confirm that our specification of 0.3 is met even in the worst case.

The entire test setup and the lens were tilted to an *EL* of 30° to evaluate the effects of the gravitational deformation of the optics system. We observed a difference of the order of 10 nm rms in the on-axis test, which is the level of change expected from the flexure. We repeated the tilt test several times and confirmed that there is no hysteresis observed. The test setup of figure 13 (except for the tilting base) was also brought to the telescope site and the equivalent results were obtained, confirming that no trouble occurred during the transportation of the WFC to the site.

3.5 Coating and the transmission

Anti-reflection coatings were applied to each element using a conventional evaporation chamber. Before the WFC assembly, we measured the transmission of each element at its center as a function of wavelengths between 370 and 900 nm. The combined transmission curve is shown as the solid line in figure 14. Outside of the wavelength range in which we did the measurements, the transmission is estimated from glass samples coated with the same parameters but in a different lot. Therefore, the uncertainty there is larger.

We built a pencil beam emitter and receiver to make direct transmission measurements of the assembled WFC. We measured at six field-angles including on- and off-axis at three different wavelengths: 405, 633, and 1064 nm. The results are averaged over the six field-angles and are shown as solid circles in figure 14. The direct-measurement results are consistent with the estimated transmission.

3.6 Focus monitor

In order to monitor focus changes, we have installed CCDs which are vertically offset by plus and minus 200 μm. We

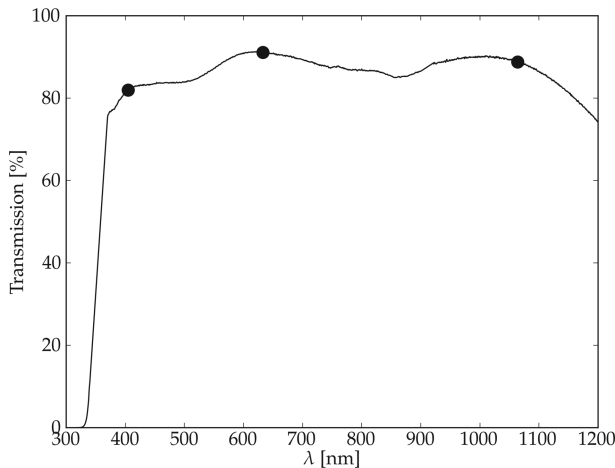


Fig. 14. Measured transmission of WFC. The three solid circles show the results of direct measurements (see text) and the solid line is the estimated values from the measurements of each element along its axis.

refer to these as the outer- and inner-focus CCDs, respectively. Four pairs of focus CCDs are arranged around the periphery of the focal plane, spaced roughly 90° apart in azimuth, as shown later in figure 16 (labeled “F”). Here we describe how we monitor the change of the focus position. When the instrument is out of focus by d the rms size of the PSF is written as

$$\sigma_{\text{PSF}}^2 = \sigma_{\text{atm}}^2 + \sigma_{\text{opt}}^2 + ad^2, \quad (3)$$

where σ_{atm} and σ_{opt} are the blurring values due to the atmosphere and optics, respectively, and a is the coefficient that depends on the optics design. For focus CCDs with an offset from the focal plane $\pm\Delta$, the rms size is written as

$$\sigma_{\pm}^2 = \sigma_{\text{atm}}^2 + \sigma_{\text{opt}}^2 + a(d \pm \Delta)^2, \quad (4)$$

$$\sigma_{-}^2 = \sigma_{\text{atm}}^2 + \sigma_{\text{opt}}^2 + a(d - \Delta)^2. \quad (5)$$

By taking the difference, d is determined as

$$d = \frac{\sigma_{+}^2 - \sigma_{-}^2}{4a\Delta}. \quad (6)$$

The parameter, a , is a function of the distance, r , from the center of the FOV, and also there is a difference between the best focus at the center of the FOV and that at the edge. Thus equation (6) can be rewritten as

$$d = \frac{\sigma_{+}^2 - \sigma_{-}^2}{4a(r)\Delta} + d_0(r). \quad (7)$$

In practice, the coefficient $a(r)$ and the best focus offset $d_0(r)$ are determined by ray-tracing of the WFC. However, estimating the σ_{+} and σ_{-} from observed stellar images requires careful treatment. First we need to de-weight the

outskirts of object images to suppress photon noise. We also need to consistently measure σ with different sizes of objects. From simulations, we found that a large, circular Gaussian weight with a fixed size (a dispersion of five pixels, $0''.84$) recovers the linear relation between the sizes in the simulation and observation. We note that the defocus estimated in this way correlates well with that obtained through the conventional focus sweep but their match is not exact. Therefore, we calibrated our defocus estimate with the one from the focus sweep once using a polynomial fitting.

4 Focal plane arrays: CCDs

The focal plane array adopted for HSC is Hamamatsu Photonics’s CCD S10892-02, which was developed in collaboration with National Astronomical Observatory of Japan (NAOJ) (Kamata et al. 2004; Suzuki et al. 2007). We employ 108 CCDs to pave the 1.5° diameter focal plane. The array was fabricated on a high resistivity ($>10\text{ k}\Omega\text{ cm}$) n-type silicon wafer which allowed full depletion across the $200\text{ }\mu\text{m}$ silicon thickness. The thickness provides enhanced quantum efficiency at longer wavelengths, reaching 40% at $1\text{ }\mu\text{m}$ (-100°C). The requirements on the CCD are summarized in table 7. In this section, we focus on the CCD specifications and their aspects of its performance that are closely related to the image quality: the packaging, the focus position, the charge diffusion, and the charge transfer efficiency. The details of the testing in the laboratory are given in a series of SPIE papers (Kamata et al. 2006, 2008, 2010, 2012, 2014).

4.1 CCD packaging

The CCD packaging is designed to satisfy our requirements on the flatness and coplanarity between mosaic CCDs. We required the global Peak-to-Valley (PV) flatness to be $35\text{ }\mu\text{m}$. “Global” means that the flatness between the bottom of the package and the light-incident surface must be guaranteed across all the mounted CCDs.

The CCD package consists of two components: a CCD base and a pin base (figure 15). The CCD base is 3 mm thick, on which the CCD die is mounted. It has a pin grid array (PGA) on the bottom side. The CCD base has a narrow slit on the CCD bonding pads so that bonding wires can be fed through the slit and wired to the pads on the CCD base. There is an inter-connection between the pads and the PGA inside the CCD base. The CCD base is made of AlN (Ariake Material).

After the processing of the CCD, the bulk silicon of the CCD wafer is mechanically polished and made thinned to the designed thickness, $200\text{ }\mu\text{m}$ in the HSC case. After the backside (light incident side) passivation process, the CCD

Table 7. Specifications of CCDs and the actual performance measured on the prototype. All measurements are made at -100°C .

Items		Requirement (-100°C)	Measured
Packaging	Format (pixel size)	$4176 \times 2048 (15 \mu\text{m} \square)$	–
	Pixel to package edge (Serial register side)	$<0.5 \text{ mm}$	0.410 ± 0.025
	Global height variation	$<5.0 \text{ mm}$	4.975 ± 0.025
		$<25 \mu\text{m}$ Peak-to-Valley	
Quantum efficiency	400 nm	$>45\%$	42%
	550 nm	$>85\%$	87%
	650 nm	$>90\%$	94%
	770 nm	$>85\%$	91%
	920 nm	$>80\%$	78%
	1000 nm	$>40\%$	40%
CTE (per pix)	Parallel direction	$>0.999995 (1600 \text{ e})$	0.999999
	Serial direction	$>0.999995 (1600 \text{ e})$	0.999998
Dark Current		$<\text{a few e hour}^{-1} \text{ pixel}^{-1}$	1.4
Charge diffusion		$\sigma_D < 7.5 \mu\text{m}$ ($400 < \lambda < 1050 \text{ nm}$)	7.5
Full well	1% departure	$>150000 \text{ e}$	180000
Amp. responsiveness		$>4 \mu\text{V e}^{-1}$	4.5
Readout noise	150 kHz readout	$<5 \text{ e}$	4.5

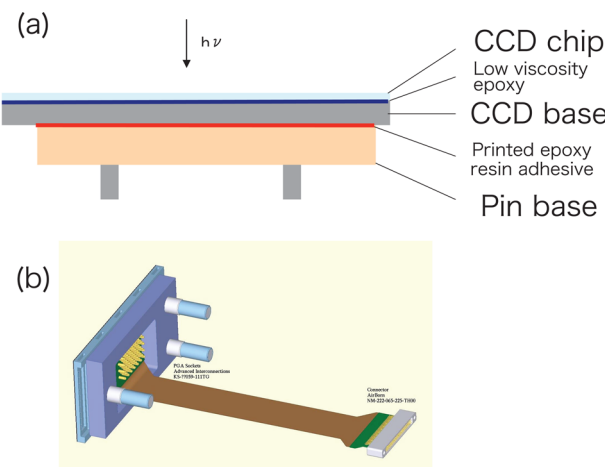


Fig. 15. Structure of CCD package (a) and its appearance (b).

die is cut out from the wafer and the die is bonded on the CCD base. The thickness variation of the CCD die is $\pm 5 \mu\text{m}$. Note that the CCD die has a natural global bow (concave toward the package) of the order of $100 \mu\text{m}$. This was minimized by applying pressure on the edge of the die while it was epoxied to the package.

The CCD die was initially bonded by a ordinary die-bond adhesive on the prototype. In order to realize better flatness, we switched to a low-viscosity epoxy paste with Si foil shims at the four corners, which is similar to what Nakata et al. (2000) worked out for Suprime-Cam. As a result, a flatness of $\sim 10 \mu\text{m}$ is realized between the CCD surface and the bottom of the CCD base in most cases.

The other package component, the pin base made of AlN, has three Ti alignment pins. Two of these pins have

tight tolerance for mounting holes on cold plates for the alignment. Each pin is machined with a screw thread which is used to mount it on the cold plate with a nut and belleville washer. This is also similar to what we developed for Suprime-Cam (Miyazaki et al. 2002). The pin base has a square aperture in the middle for the feed-through of a flex cable. The pin base is epoxied to the CCD base and the uniformity of the thickness of the epoxy resin adhesive is $\text{PV} = 2 \mu\text{m}$ which is realized by using a screen printing method. The adhesive is cured thermally.

After inspection, it turned out that the absolute thickness of the CCD base has a large scatter of $\pm 8 \mu\text{m}$ between individual pieces, even though the flatness on each piece met the specification of $\pm 5 \mu\text{m}$. On the other hand, the scatter of the pin base thickness was well controlled among the pieces ($\pm 2 \mu\text{m}$). Therefore, we decided to procure thicker- and thinner-pin bases over a $\pm 10 \mu\text{m}$ range. Then, the appropriate combination of the CCD base and the pin base was determined based on measurements of the heights of the bases. Thus, we minimized the scatter of the total thickness down to $\leq 8 \mu\text{m}$ in most cases.

The CCD height measurements were made on individual devices at room temperature using a laser displacement meter (Mitaka Koki NH3-SP with an accuracy of $\pm 1 \mu\text{m}$) and the 116 measured results are tiled in figure 16, although the height difference of the eight focus CCDs (subsection 3.6) is $200 \mu\text{m}$ and out of the height range shown here. After we examined the height of each device, we noted that heights 15–20 CCDs are systematically higher than those of the others by $\sim 15 \mu\text{m}$. This is caused by the fact that we could not find an optimal combination of the

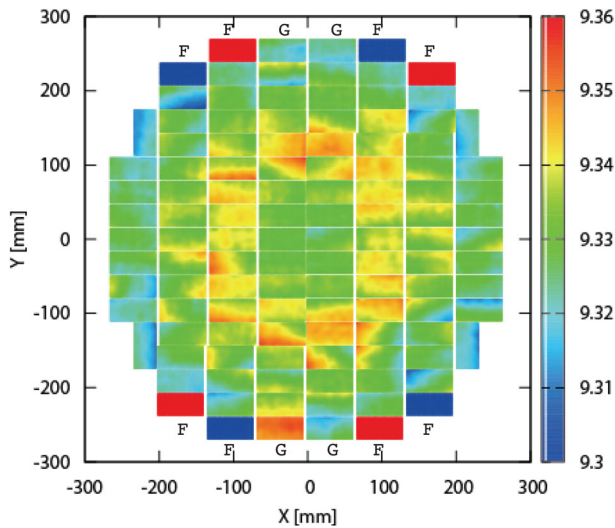


Fig. 16. Laboratory measurement of CCD height variation at the room temperature. The vertical scale is in units of mm. The four CCDs labeled “G” are used for the autoguider whereas the eight CCDs labeled “F” are for focus CCDs. The remaining 104 CCDs are used for science imagings.

pin base and the CCD base in every case due to the limited stock of parts. We decided to put those CCDs at a position where the deviation from the flat focal plane due to the field curvature is at its maximum. This can be seen in the rim of CCDs at $r \sim 90$ mm. We also note that some CCDs have a flatness error larger than $40 \mu\text{m}$. Because this appears as a slope of the height and the spatial frequency is small, this can be explained by residuals in the CCD die’s bow correction while it was epoxied on the CCD base. Because the sensitivity to the local z error is relatively large (subsubsection 2.2.4), a Δz of $40 \mu\text{m}$ causes $\Delta\text{FWHM} > 0''.168$ which would be visible under the good seeing condition. The existence of the large height jump requires that PSF modeling of the image must be made locally in each CCD device.

4.2 Best focus position

The absorption length of a $1 \mu\text{m}$ photon in silicon is about $320 \mu\text{m}$ (-100°C), which is larger than the thickness of the CCDs. Therefore, the best focus position, where the minimum size of the image is realized, is deeply inside the silicon. We carried out a simple image simulation to locate the best focus position. Photons of $F/2$ beam are generated and is incident on the silicon. The position of the absorption is determined given the absorption length at that wavelength (figure 17). By changing the height, we search for the best focus position at which the charge spread is minimized. Table 8 summarizes the results for an Si thickness of $200 \mu\text{m}$. At wavelengths of 700 nm or below those, the absorption occurs right under the surface, whereas at

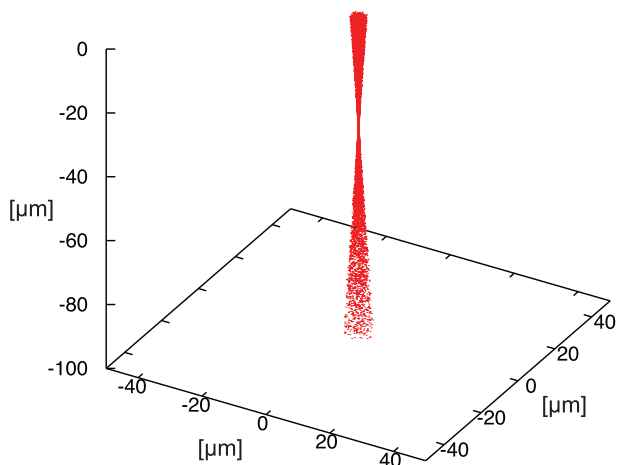


Fig. 17. Position of the absorption of $F/2$ beam photons ($\lambda = 900 \text{ nm}$) inside silicon. The thickness of silicon is set at $200 \mu\text{m}$. The focus position of the incident light is set at $43 \mu\text{m}$ below the surface where the minimum image size is realized.

Table 8. Best focus position from the incident surface in each wavelength.

$\lambda [\text{nm}]$	Focus pos. [μm]	$\sigma [\mu\text{m}]$	FWHM [$''$]*
700	5.9	0.20	0.006
800	14.3	0.48	0.013
900	43.0	1.36	0.036
1000	89.7	1.98	0.052

*The Si thickness of $200 \mu\text{m}$ is adopted here. On-axis $15 \mu\text{m}$ pixel scale is $0''.168$.

$\lambda = 1 \mu\text{m}$, the best focus position is nearly halfway through the thickness of the device.

Image spread due to the absorption of the fast $F/2$ conic beam has been a concern. Table 8 shows the rms spread of the image, which is very small compared with the $15 \mu\text{m}$ pixel size. This is because silicon has a high refractive index and the beam becomes much slower ($>F/7$) inside the silicon. The actual image spread is determined by charge diffusion, as we argue in the following subsection.

4.3 Lateral charge diffusion

In back-illuminated CCDs, photon-generated charges drift due to the electric field inside the depletion layer down to the potential well under the electrodes. During the transverse drift, the charges suffer from lateral spreading which causes the image to smear. This charge diffusion can be serious for shorter-wavelength photons which are absorbed near the surface, and thus the charges they generate travel a longer transverse distance.

The expected charge diffusion is $\sigma_D = 7 \mu\text{m}$ for the transverse distance of $200 \mu\text{m}$ at -100°C (Janesick 2001). The actual vertical distance depends on where the photon is

Table 9. Same for table 8 but charge diffusion is considered here.

λ [nm]	Focus pos. [μm]	σ [μm]	FWHM [$''$]
700	5.6	6.9	0.18
800	19.2	6.6	0.17
900	43.8	5.8	0.15
1000	84.7	4.5	0.12

absorbed. We took the charge diffusion into account in the simulation and the position of the charge is laterally shifted by $7 \times d_t/200 \mu\text{m}$, where d_t is the transverse travel distance. Table 9 shows the image size when we taking the charge diffusion into account. At shorter wavelengths, the image size is determined mostly by charge diffusion, as expected. As the wavelength becomes longer, the image size gets smaller because the transverse travel distance tends to be shorter. Note that the position of the best focus does not change much compared with the cases where the charge diffusion is ignored (table 8).

We also directly measured the image smear due to the charge diffusion (Kamata et al. 2008). A pin-hole of $10 \mu\text{m}$ diameter was reduced by 1/10, and was projected on the CCD using an objective lens. The lens's numerical aperture (NA) of ~ 0.25 was selected to mimic the $F/2$ beam. The size of the resulting image was measured by simple Gaussian fitting implemented on IRAF/imexam. Note that the imaging system is fairly under-sampled, considering the pixel size of $15 \mu\text{m}$. We checked on the imexam fitting results with artificially generated Gaussian images of various sizes. The imexam's results agreed with the input σ within 5%–10% down to one third of the pixel size, as long as the image center was close to the center of a pixel. Aligning the centers of the pin hole spot and the pixel was easy to do by balancing the values of neighboring pixels.

Figure 18 shows the results of the measurement. The CCD has a electric structure which keeps the backside (light incident side) positively biased to minimize the diffusion. When we set the backside bias voltage to $V_{\text{BB}} > 40 \text{ V}$, the PSF is smaller than half the pixel size at both blue and red wavelengths. The horizontal lines show the expected image size calculated from the image simulation assuming a charge diffusion of $\sigma_D = 7 \mu\text{m}$ over the $200 \mu\text{m}$ thickness. The measurement is consistent with what was expected from the simulation. We could expect an even smaller PSF if we increase V_{BB} further. However, the readout amplifier starts to glow if we set $V_{\text{BB}} > 50 \text{ V}$, contaminating the imaging area. Therefore, we operate the CCDs under 50 V .

In the prototyping phase of the fully depleted CCD, Hamamatsu demonstrated that a thickness of $300 \mu\text{m}$ is feasible. A thicker CCD gives higher quantum efficiency, but has more charge diffusion. We decided to employ CCDs

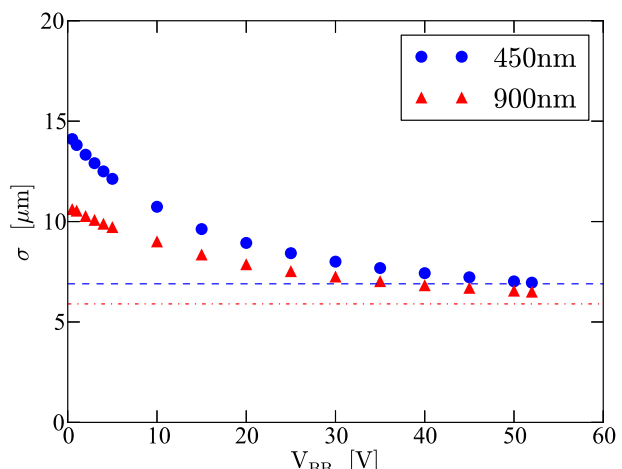


Fig. 18. Charge diffusions as a function of the applied back bias voltage at two wavelengths (filled circle: 450 nm; triangle: 900 nm). The dashed line and dot-dashed line show the expected spreads obtained from the simulation at the two wavelengths, respectively. (Color online)

with a thickness of $200 \mu\text{m}$ after the actual measurement of the charge diffusion: we judged that $\sigma_D \sim 7.5 \mu\text{m}$ was acceptable in the image error analysis.

4.4 Charge transfer efficiency

When the charge is transferred by clocking for readout, a fraction of the charges can be trapped and lost (or released later on). The fraction of electrons that are moved from one pixel to another on readout is described by the charge transfer efficiency (CTE). Poor CTE could smear the PSF and, in fact, the CTE is degraded significantly in space environments and needs to be corrected in the image processing (Massey et al. 2010). The CTE is measured using X-rays. X-ray photons generate multiple electron-hole pairs, and the number of pairs is proportional to the energy of the incident X-ray photon (3.65 eV per pair). Thus, a line X-ray from a radio isotope is a useful calibrator because the amount of input charge is known.

After the illumination of the line X-rays, we read out the image, and searched for the X-ray events that were created by the absorption of the X-rays. Typically, in the case of the thick back-side illuminated CCDs like ours, the X-ray events are spread among multiple neighboring pixels. Thus, we sum up those signals to record the pixel values of the event. Figure 19 shows the result of the analysis. Each dot corresponds to each detected X-ray event. The horizontal axis shows the location of the X-ray event in the parallel (left-hand panel) and serial (right-hand panel) directions. This corresponds to the number of transfers. The vertical axis shows the summed pixel values of the event.

The two visible bands represent the lines of the ^{55}Fe source (5.9 keV and 6.2 keV). If CTE is 100%, the band

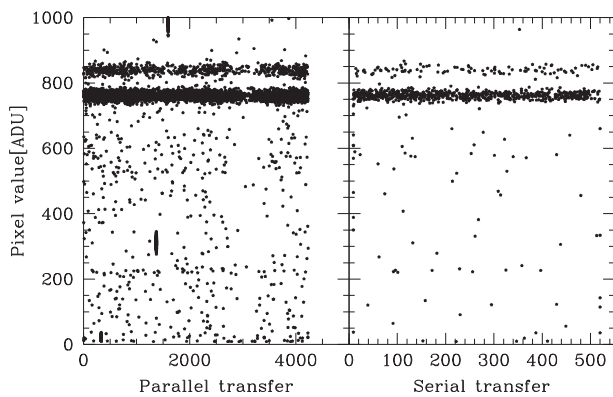


Fig. 19. Scatter plot of X-ray events. The horizontal axis shows the location of the X-ray event in the parallel (left-hand panel) and serial (right-hand panel) directions. The vertical axis shows the pixel values of the event.

will stay in the horizontal direction, but the CTE is poor, with the band tilted due to more loss of charges on pixels further from the amplifier. Thus, the slope of the bands (α) is an estimator of the CTE. The CTE η is calculated as $\eta = (N\alpha)^{1/N}$, where N is the number of transfers. The estimated parallel and serial CTEs are 0.999999 and 0.999998, respectively. Practically no image smear is expected with such a good CTE.

5 Camera unit

There are numbers of papers already published by members of the HSC development team describing various aspects of the HSC camera unit. Here we present a brief overview of the units and give appropriate references.

The focal plane is installed in a cryogenic dewar. The operation temperature of the CCDs is -100°C , at which the dark current is completely negligible. Because the quantum efficiency at longer wavelengths has a temperature dependence, we put a tight specification on the temporal variation of the temperature: peak-to-peak $<0.5^{\circ}\text{C}$. The cooling is realized by two pulse tube coolers, custom-developed by Fuji Electric, the thermal performance of which is measured to be 50 W each at -100°C . In order to keep the necessary vacuum level, we have installed an ion pump with $20 \ell \text{ min}^{-1}$ performance. The details of the mechanical and thermal design of the camera dewar and its actual performance are presented by Komiyama et al. (2010), Obuchi et al. (2012), and Komiyama (2017). On the focal plane, we installed 116 CCDs. One hundred and four of these are used for science imaging. Four CCDs are used as autoguiders and eight CCDs are used to measure the focus displacement (subsection 3.6). The CCD readout electronics was developed in-house at NAOJ (Nakaya 2012) in collaboration with the high energy physics groups at the High Energy

Accelerator Research Organization (KEK) and the University of Tokyo. The CCD clock-drivers, the preamplifiers, the dual slope integrator, and the analog-to-digital converters are all implemented on the front-end electronics (FEE) PC boards which are installed inside the dewar. The back-end electronics (BEE) are located outside the dewar. They feed the digital signals for clocking and deliver power to the FEE through hermetic connectors. Digital signals from the ADC come back to BEE system. The core of the BEE is a Field-Programmable Gate Array (FPGA)-based Transmission Control Protocol (TCP) processor (Uchida 2008) which was custom-built for the HSC (Uchida et al. 2012; Miyatake et al. 2012). The data acquisition (DAQ) computer is linked with the BEE via giga-bit ethernet and stores images on the local hard drives. The pixel rate of the CCD is set to 135 kHz and it takes 20 s to read out the CCD through the four amplifiers. The measured readout noise is 4.5 electrons at the telescope. In order to handle the massive data (1.8 GB), we introduce two identical sets of BEE and the DAQ computers, each of which handles half of the CCDs. The dead time between exposures is 34 s, which includes time for the CCD wipe, CCD readout, and storing the data on the Redundant Arrays of Inexpensive Disks (RAID) hard drives. For details of the CCD readout electronics, we refer the reader to a series of papers published in SPIE proceedings (Nakaya et al. 2006, 2008, 2010, 2012).

The four CCDs for the autoguider are located at the outer edge of the mosaic (Morokuma et al. 2008). The four CCDs have a dedicated FEE, BEE, and DAQ computer system so that they can be read out independently from science exposures. Using star catalogs and the camera-pointing information, we identify a suitable star for guiding. We partially read out a rectangular region of the CCD every 0.5 to a few seconds. While reading out, the exposure continues. This gives rise to tails on the star's image along the charge transfer direction, which gives a fixed offset to the determination of the star location. This is, however, harmless for the guiding. Because the auto-guider CCD is behind the shutter, we do not start guiding the telescope until the position of the star is measured. We usually have a lag of roughly 4 s before the start of the guiding.

The SH waveform sensor for the mirror analysis consists of a collimator and a 16×16 micro-lens arrays (MLA). We install these components inside the filter frame and it is loaded using the filter exchanger described below. Inside the filter frame, we put a 45° mirror in the beam. It is then collimated by a collimator and fed into the MLA. The output micro beams from the MLA are again reflected by another 45° mirror and projected onto one of the science CCDs. This gives us a compact SH system which fits into the filter frame. The collimated beam is split by a dichroic

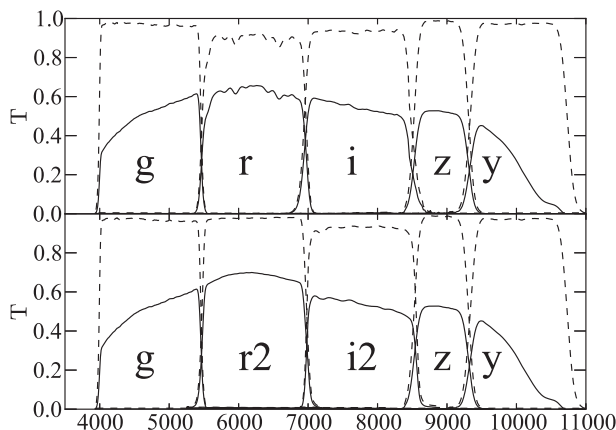


Fig. 20. Filter transmission functions of the five standard broad-band filters (dashed lines) and their total system throughput (solid lines). The bottom panel shows the transmission function and the throughput of the newly built r_2 and i_2 filters.

mirror which is fed into a commercial video camera. This is used for guiding the telescope during the exposure for the mirror analysis. The details of the SH sensor are given in Morokuma et al. (2008).

The filter diameter and its clear aperture are 600 mm and 560 mm, respectively. The optical specification of the HSC filters basically follows that of Suprime-Cam; 50% cut-on/off wavelength error <10 nm, peak transmission $>90\%$, and out-of-band leak $<0.5\%$. With the exception of the z band, the broadband filters of Suprime-Cam were composed of a combination of a colored glass (lower wavelength cut) and a glass with a multi-layer interference film coating (upper wavelength cut). Because there was no colored glass available for the large size needed for the HSC filters, the lower wavelength cut in the HSC filters is also realized with multi-layer coating. We built five 100–150 nm width broadband filters, called HSC- g , HSC- r , HSC- i , HSC- z , and HSC- y (g , r , i , z , and y for short), which are similar to the SDSS filter system (Fukugita et al. 1996). The dashed lines in figure 20 show the transmission curves of the broadband filters. The r and i filters were built in the early phase of the camera development and the spatial uniformity of the cut-on/off wavelength did not meet our specifications. We observed radial variations ranging over 7 nm. When we divided a night sky image with a flat field image generated from the flat field screen, we saw a radial ripple of a few percent. This was caused by the difference of the spectrum between the night sky and the flat screen coupled with the radial variation of the filter transmission. Thus, we replaced the r and i filters; the new filters are called r_2 and i_2 (bottom panel of figure 20). In addition, more than 10 narrow-band filters of 15 nm width have been built. The typical spatial variation of the 50% cut-on/off wavelength is 3 to 4 nm for the narrow-band filters. The details of the HSC filters

are described in Y. Kawanomoto et al. (in preparation). The filter exchanger unit (FEU) consists of two parts: the “central unit” that holds a filter in the light beam, and the “stacker unit” which stores the filters. The central unit is located between the dewar and the shutter and it has a precision alignment mechanism that guarantees 10 μm position stability with respect to FP. The stacker is a jukebox of the filters. The transfer of a filter between the stacker and the central unit is realized by a motorized cart installed inside the stacker unit. The cart, in combination with a mechanical latch, provides the push/pull mechanism. We have two identical stacker units and each stores three filters. The stacker unit is installed outside of the POPT2 and is usually folded up vertically by mechanical actuators (figures 1 and 2) to reduce the vignetting of the incident light at M1. When a filter is exchanged, the stacker is deployed horizontally. It takes 16 min to complete one exchange cycle. In actual operations, we point the telescope to the zenith and close the M1 cover while exchanging filters for safety, because mechanical troubles of the FEU might cause fatal falling objects onto M1. This requires another 10–15 min. Therefore, it takes nearly 30 min to exchange filters at the moment.

Because the number of available filters is larger than the number of filter slots (six) in the stacker, we select the set of filters and load them in the slot before an observing run starts. This gives rise to operational constraints at the time of writing. However, FEU stackers can be detached from the POPT2 without uninstalling the entire HSC from the telescope. The observatory will soon implement a procedure to swap the filters in the slots during the daytime, in the middle of observing run.

The shutter mechanism is a roll screen, because the space constraint for the 600 mm diameter shutter aperture was tight. The screen we employed is a commercial product for a blind screen. The material is a fiberglass sheet laminated with black polyvinyl chloride. The thickness is 0.3 mm and the transparency is less than 6×10^{-6} from 300 to 1060 nm. Two screen rolls are installed on both sides of the aperture and the leading edge is fixed on a metal bar which is driven with a ball-screw mechanism. The axis of the roll is also driven by the same motor. The tension on the screen is realized by a spring installed in the axis of the roll. The spring also absorbs the difference of the linear motion and the rotation angle accruing from the change of the radius of the roll during the winding of the screen. For normal operation, one screen is wound up to open the aperture and the other screen is pulled out to close it. Because it takes 1.2 s to move across the aperture, the minimum exposure time for the HSC is set at 2.0 s. The maximum deviation of the shutter time is measured to be 0.01 s. Details of the FEU and the shutter are given in Uraguchi et al. (2012).

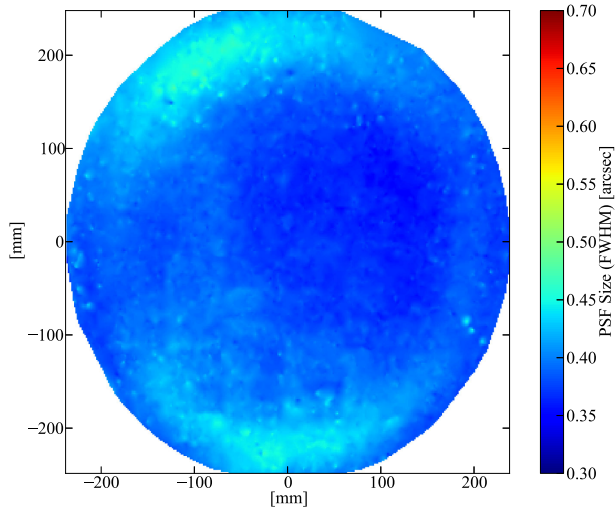


Fig. 21. PSF size variation over the field of view ($<\phi 1.5$) in the HSC-*i* band. The exposure time and the elevation are 200 s and 72° , respectively. The PSF size is $0''.36$ at the center.

6 Performance verification

6.1 System throughput

Figure 20 shows the measured transmittance of the five broad-band filters (dashed lines). Multiplied by the CCD quantum efficiency, the transmittance of the dewar window, the wide-field corrector, and the reflectance of the primary mirror, we obtain the calculated throughput of the camera, shown by the solid lines. The transmittance of the newly built *r* and *i* filters are shown in the bottom panel. We note that the cut-on/-off wavelengths have changed from the HSC-*r* and HSC-*i* filters to the *r2* and *i2* filters respectively and care should be taken in handling the combined data.

The average throughputs in the HSC-*g*, *r2*, *i2*, *z*, and *y* filters are 0.46, 0.53, 0.42, 0.36, and 0.18, respectively. Not included in these plots is the vignetting of the WFC (figure 9). We observed the spectrophotometric standard stars GD153, with HSC-*g* and HSC-*z* filters, and GD71, with the HSC-*i* filter, on a potentially photometric night and confirmed that the observed fluxes match well with the expected ones within 5% to 10%. This also requires an understanding of the transparency of the atmosphere. Therefore, we conclude that the absolute system throughput shown in figure 9 is a reasonably good estimate.

6.2 Measurement of the PSF

We characterize the PSF of the camera using stellar images from an exposure. The pixel scale at the center of the field of view is 0.169 [arcsec pixel $^{-1}$]. Figure 21 shows the spatial variation of the PSF FWHM estimated roughly from the

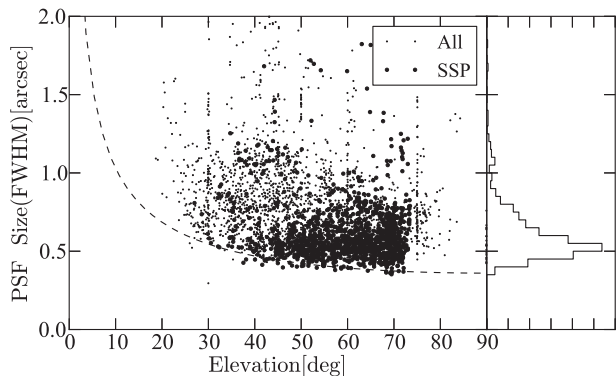


Fig. 22. HSC-*i* band PSF size at the field center versus elevation taken from 2014 February to 2016 January. Thick filled circles are from the coordinated SSP data and thin ones are from all exposures. The dashed line is the function $0.36\sin^{-3/5}(EL)$ which is the expected elevation dependence of the natural seeing. The histogram in the right-hand panel shows the seeing statistics of the SSP data whose median value is $0''.56$, whereas the median value of all the data is $0''.69$. The vertical clusters of data points at $EL = 30^\circ$, 60° , and 75° are from a test observation run collecting for characterizations of the HSC.

flux-weighted second moments, I_{xx} and I_{yy} , of stars under the assumption that the PSF is circular:

$$s = 0.169 \times 1.67 \times \sqrt{\frac{I_{xx} + I_{yy}}{2}}. \quad (8)$$

This exposure was taken under superb conditions and the PSF size at the center is $0''.36$ (FWHM). Note that the PSF remains well-sampled even under such good seeing. The PSF gradually increases from the center to the edge which is explained, in part, by the change of the pixel scale toward the edge as explained in sub-subsection 3.2.1. We also have an increase of the optical aberration from the center but the aberration decreases close to the field edge because of the vignetting. This explains the circular ring structure visible in figure 21. We also note that the variation is not axially symmetric. This suggests that the optical system is somewhat mis-aligned. We assess the origin and stability of the asymmetry in subsection 6.3.

The PSF varies over time due to changes in the natural atmospheric seeing. Figure 22 shows the HSC-*i* band PSF size monitored over two years as a function of the elevation of the telescope. Data from the SSP are shown by thick circles. For the SSP, HSC-*i* band images have been taken preferentially under better seeing conditions. The median PSF size for the SSP data is $0''.56$ (FWHM), and is $0''.69$ for all the data.

The elevation dependence on the seeing expected from the Kolmogorov nature of atmospheric turbulence is represented as $s_z \sin^{-3/5}(EL)$ (Roddier 1981), where s_z is the seeing toward the zenith. The dashed line shows the expected elevation dependence where we set $s_z = 0.36$. This nicely follows the lower envelope of the data points.

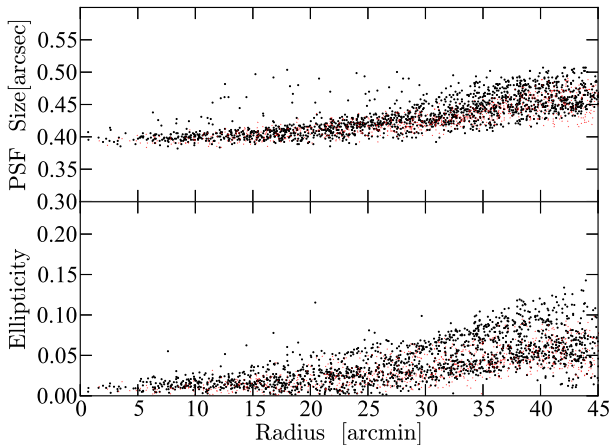


Fig. 23. (a) PSF size (FWHM in arcsec) of stellar objects and (b) the ellipticities as a function of the field angle. Black points are taken from an actual *i*-band 200 s exposure data with the $EL = 70^\circ$. Red points are the sizes and the ellipticities of the calculated PSF assuming a 0.36'' free-air Gaussian seeing. The optics model that incorporates the known manufacturing errors and measured wavefront errors is used. In the model, the POPT2 is tilted by 20'' with respect to the M1 optics axis which results in a good match between observations and the calculation.

Changes in elevation could cause collimation errors, resulting in image degradation. However, we see no evidence for such image degradation in the figure. This suggests that the collimation system works as designed and the alignment error is well controlled. If we assume that the best natural seeing in the HSC-*i* band is 0.36'', we could argue that the instrument PSF is smaller than 0.36'', which is consistent with the estimate made in the design (table 2). Note the sparsity of data at high elevations ($EL > 73^\circ$). This is because observers are usually advised to avoid such high elevations because the PSF becomes worse due to larger drive errors of the instrument rotator.

6.3 Understanding the PSF

Next, we analyze the field-position dependence of the PSF to evaluate whether the HSC opto-mechanical system satisfies the design specifications. Figure 23 shows the radial dependence of the PSF size (top) and the ellipticities of the PSF (bottom) that are calculated from the weighted second moments as

$$e_1 = \frac{I_{xx} - I_{yy}}{I_{xx} + I_{yy}}, \quad e_2 = \frac{2I_{xy}}{I_{xx} + I_{yy}} \quad (9)$$

Black points present the observed values taken under relatively good seeing ($\sim 0.4''$). The red points in the figure show the model results calculated from the optical ray-tracing convolved with a free-air Gaussian seeing of 0.36''. In the model calculation, we had to tilt the camera system by 20'' with respect to the axis of the primary mirror to match with the observed results. This suggests that we still had an

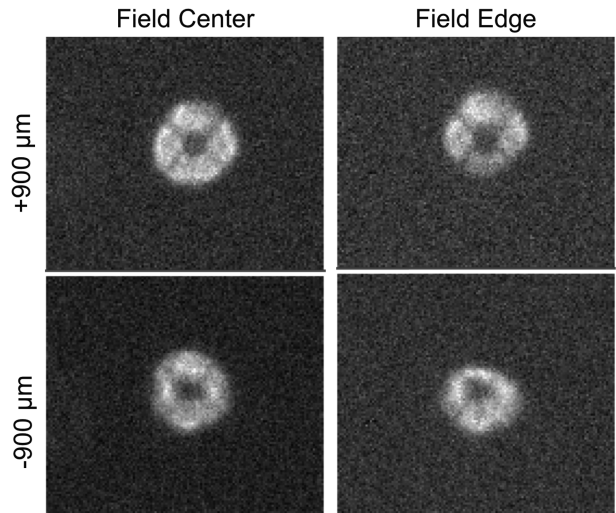


Fig. 24. Images that are out of focus by $\pm 900 \mu\text{m}$, taken at the field center and near the field edge. The vignetting of the aperture is visible on the field edge.

opto-mechanical alignment error of 20'' when we took the data shown here.

In order to characterize the behavior of the PSF more systematically, we obtained a pair of off-focus images with a displacement of $\Delta z = \pm 900 \mu\text{m}$. Figure 24 shows the donutlike appearances of the images where the spider of the telescope top ring and POPT2 are visible. Because the WFC has vignetting, the occultation is seen in the images near the field edge. This occultation is only seen on either one of the focus positions ($-900 \mu\text{m}$ in this case) depending on the field position (x, y).

We can calculate the expected inner and outer off-focus images, $\hat{I}(x, y)$, using the perfectly aligned optics, where the hat “ $\hat{\cdot}$ ” indicates “designed” values. The Zernike coefficients of the designed image, \hat{a}_i , are defined as

$$\hat{I}(x, y) = \left| \mathcal{F} \left\{ \exp \left(\frac{2\pi i}{\lambda} \sum_{i=2}^{16} \hat{a}_i Z_i(u, v) \right) \right\} \right|^2, \quad (10)$$

where \mathcal{F} stands for the Fourier transform on the pupil plane, (u, v) . We truncated the coefficients at the order of 16, beyond which the convergence of χ^2 fitting got worse. The actual system has manufacturing errors and alignment errors which cause wavefront errors, Δa_i :

$$\Delta a_i = a_i - \hat{a}_i, \quad (11)$$

where a_i are the Zernike coefficients of the observed image.

Here we are primarily interested in Δa_i to understand the system. The estimation is done in real space using the ray-tracing calculation. After adding a unit value for \hat{a}_i to the pupil plane, we calculate the image, and subtracting the model $\hat{I}(x, y)$ gives us the impact of the change of a_i , which

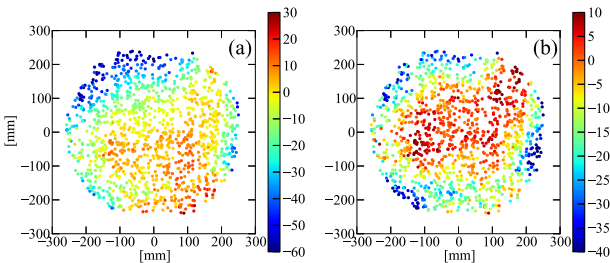


Fig. 25. (a) Map of defocus in μm estimated from Δa_4 . The units of the 2D plane is mm. (b) The global tilt of the map is subtracted to see the residual defocus on the focal plane. Note that the color scale is different in the two images.

can be used as a basis vector for the parameter estimation. By minimizing the difference between the observed image and the calculated image, we are able to estimate a set of Δa_i .

This forward-fitting approach is necessary for properly including the vignetting in the analysis. Thus, we obtain the Zernike coefficients of the pair of outer (+, away from the primary mirror M1) and inner (-, closer to the M1) foci, Δa_i^+ and Δa_i^- respectively. By averaging these two, we estimate the wavefront error at the $z = 0$ position as

$$\Delta a_i^0 = \frac{\Delta a_i^+ + \Delta a_i^-}{2}. \quad (12)$$

In what follows, we omit the superscript 0 for simplicity.

The defocus is estimated directly from Δa_4 . Figure 25a shows the defocus map which is obtained in a moderately dense stellar field in an HSC-*i* band 60 s exposure. In the figure, we see the global piston and tilt which are thought to be due to the alignment error in this particular exposure with respect to the perfectly aligned optics.

Substituting the best-fitting piston and tilt, we obtain the intrinsic residual defocus which is shown in figure 25b. At the center we have a 10–15 μm level, diagonally aligned residual which is thought to be due to the height difference across the CCD boundary. Comparison with the measured height variation (figure 16) is interesting. We arranged the CCDs so that the surface roughly follows the field curvature of the optics. The effect of the arrangement is suggested by the flat plateau near the optical center seen in figure 25b. However, we see a 10–15 μm depression in the surrounding outer region where we should have raised the height of CCDs. Because the selection of the CCD heights was limited, this prevented us from building a completely ideal focal plane surface.

In order to evaluate the alignment errors, we model Δa_4 as a linear function of the field position (x, y):

$$\Delta a_4(x, y) = \Delta a_4(0, 0) + \Theta^x y + \Theta^y x, \quad (13)$$

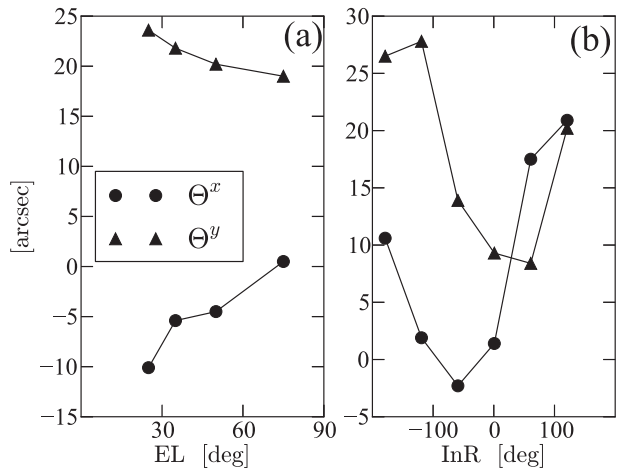


Fig. 26. Elevation dependence of the global tilt of Δa_4 map (a) and its InR angle dependence (b).

where (Θ^x, Θ^y) are the tilt angles with respect to the (x, y) axes, and $\Delta a_4(0, 0)$ is the defocus at the center of field of view. We obtained a series of off-focus images by changing the elevation of the telescope and the instrument rotator angle in order to characterize the flexure of the camera mechanics through the variation of (Θ^x, Θ^y) . Figure 26a shows the elevation dependence where an $\sim 10''$ increase of the Θ^x (tilt) is visible as the telescope points away from the zenith. This is a result of flexure due to the change of the gravity direction. The sign of the effect tells us that the WFC side comes closer to the ground, which is what we expect because this side is heavier. This tilt is roughly consistent with the flexure of LF as described in sub-subsection 2.2.4.

The instrumental rotator angle dependence is shown in figure 26b. Clear 2π cycle sine curves are seen. The offset from the origin and the amplitude are roughly 8.3 ± 12 and $17.7 \pm 10.7 ["]$, respectively. The offset shows the alignment error of the instrument rotator axis with respect to the M1 optic axis and the amplitude shows the alignment error between the rotator axis and the CCD focal plane. In subsubsection 2.2.4, we estimated that a tilt of the order of $10''$ is expected for a 1 m diameter structure considering the standard manufacturing error of $50 \mu\text{m}$. We have at least four components involved: the lens frame, the instrument rotator, the dewar frame, and the structure inside the dewar. The error observed here is roughly consistent with what is expected from the manufacturing and setting errors of these four components.

The tilt of the WFC and the focal plane with respect to the major optical axis is also measured independently through the astigmatism. As shown in figures 7 and 8, the stellar images are slightly elongated radially (tangentially) as the z position of the focal plane increases (decreases). Therefore, when the center of the field is located at the

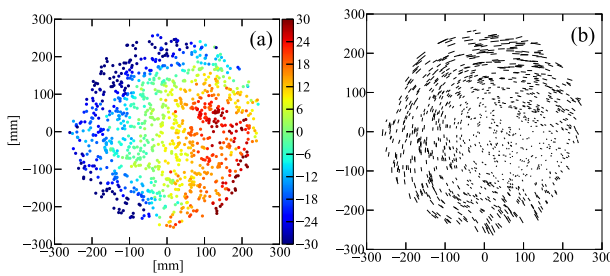


Fig. 27. Defocus (Δa_4) map (a) and the astigmatism map (Δa_5 , Δa_6) (b).

designed focus position and the focal plane is tilted, we observe a coherent elongation pattern over the field of view as shown in figure 17 of Miyazaki et al. (2002). When both the WFC and the focal plane tilt together, we observe a similar elongation pattern due to the astigmatism. In the early phase of the optics alignment, we characterized the shape of the PSF as a simple ellipse and the degree of the elongation is measured by its ellipticity. By changing the tilt angle using the hexapod, we searched for the angle at which the coherent ellipticity pattern is minimized. Thus, we could roughly align the optics but the accuracy is limited to around 1', because as it approaches the best value, the elliptical approximation for the PSF becomes less appropriate. The tilt measurements using Δa_4 are more sensitive as mentioned above. Figure 26 suggests that the alignment precision is now better than half an arcminute.

The Zernike coefficients of Δa_5 and Δa_6 are a measure of astigmatism. For the exposure taken at the instrument rotator angle of -120° shown in figure 26b, the variation of the astigmatism over the field is presented as a whisker plot in figure 27b, where the length of the whisker is proportional to $\sqrt{\Delta a_5^2 + \Delta a_6^2}$ and the position angle is calculated as $2\tan^{-1}(\Delta a_6/\Delta a_5)$. Figure 27a shows the map of Δa_4 of this exposure. As expected, we see radial elongation in regions with positive defocus and tangential elongation in regions with negative defocus.

Next, in order to cross-check the measurements by the donut analysis (figure 24), we analyzed images from the outer and inner focus CCDs. But in this case, the z offset value of $200\text{ }\mu\text{m}$ is small and not ideal for the wavefront analysis. Therefore, we summed up (after flux scaling) all the star images and evaluated the Zernike coefficients of the summed images assuming that the spatial variation of coefficients in a single CCD is negligible. Also, we only adopted coefficients up to sixth order here because the inclusion of higher-order terms made the fitting unstable. We averaged the two coefficients on a neighboring pair of inner- and outer-focus CCDs as in equation (12) to obtain an estimate of the coefficient at the averaged location. Because we have four pairs of inner- and outer-focus CCDs, one exposure provides the wavefront error estimate at the four locations along the outer edge of the field of view.

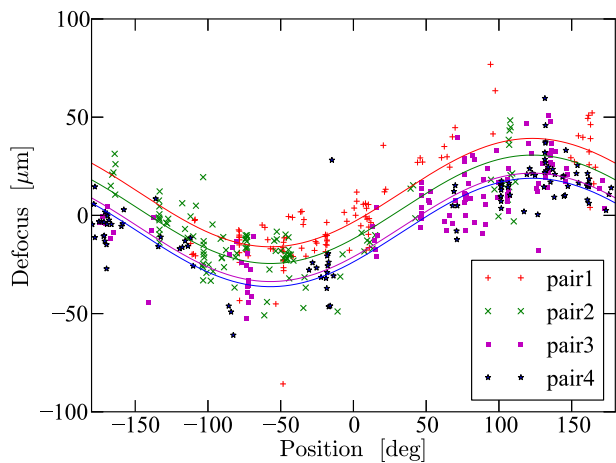


Fig. 28. Defocus (Δa_4) estimated from the four pairs of inner- and outer-focus CCDs from 104 exposures on the night of $0.^{\circ}73$ median seeing. Solid lines show the best-fitting sinusoidal curve to the data where we assume a common phase and common amplitude.

We analyzed 104 exposures in the HSC-*r2* band taken on one night with a median seeing that was moderately good ($0.^{\circ}73$ in FWHM). Figure 28 shows the defocus (Δa_4) as a function of the azimuthal position of the pair of focus CCDs during the exposure. Each pair of CCD data can be fitted well with sinusoidal curves that have common phases and amplitudes, but different offsets. This variation can be explained by the misalignment of the instrument rotator axis and the CCD focal plane. The offsets from one pair to another reflects the difference of the average height of the focus CCDs. The amplitude of the sinusoid is $23\text{ }\mu\text{m}$, which is roughly consistent with what is estimated from the donut analysis (figure 26b), where we observed $\sim 12''$ amplitude for both (Θ^x, Θ^y) . The total tilt is calculated as $\sqrt{2} \times 12''$, which corresponds to $20\text{ }\mu\text{m}$ for the radius of the focal plane (250 mm). Note that we will be able to correct the misalignment of the rotator axis and the focal plane by shimming, and this will eliminate the sinusoid in figure 28. This is planned, but has not yet been carried out because the tilt is smaller than the specification and thus the impact on the image quality is limited.

In this subsection, we showed the results of wavefront error analysis based on off-focus stellar images in order to understand how our PSFs are formed. We observed the variation of the defocus component when we changed the telescope elevation and the instrument rotator angle. These are consistent with the expected collimation error which was estimated in sub-subsection 2.2.4). We also confirmed that arranging the mosaic CCD heights to follow the field curvature of the optics was partially successful at least at the field center but was not optimized in the outer field region. These findings will be useful when we build PSF models in analyzing data in sparse high-latitude fields in which the number of stars available to measure the PSF is limited.

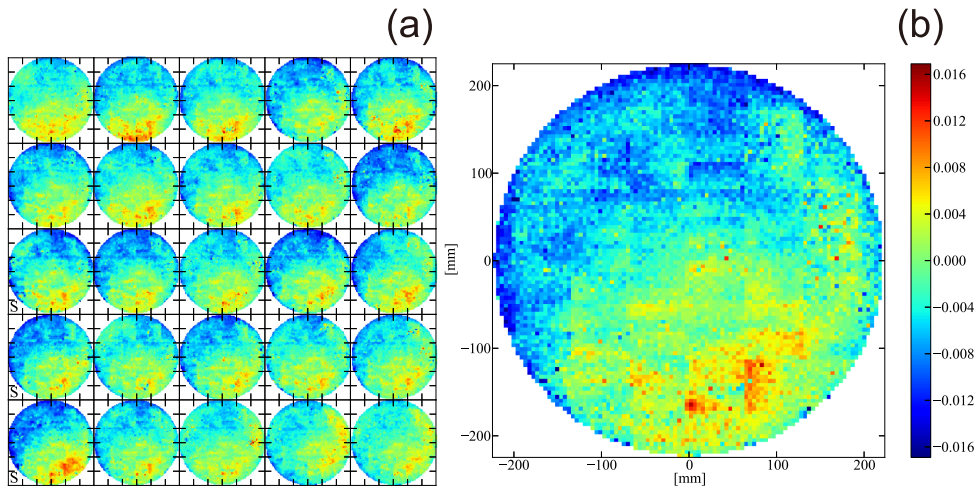


Fig. 29. (a) A series of PSF residual maps, the exposures of which were subsequently made over one hour (starting from the top left-hand panel and continuing to the right and down). The exposure time of each image is 150 s, except for the three exposures (30 s) at the lower left-hand corner labeled “S.” (b) An average of the 25 residual images on the left. The PSF size residual from the model is represented in arcseconds.

6.4 PSF on science exposures

Finally, we evaluate the spatial and temporal variations of the PSF size of on-focus science images that exposure times usually longer than 120 s. We use moderately bright stars ($18 < r < 22$) as control stars to evaluate the PSF of the image. The typical number density of such control stars is roughly 40–50 per CCD depending on where the telescope points to.

In weak lensing analysis, we need to model the PSF accurately in order to measure the lensing signal in faint galaxies. Systematic errors in the PSF will be imprinted in the weak lensing signal. If the number density of the control stars is not sufficient to follow a spatial variation of PSF, the PSF modeling would be imperfect. It would be ideal if we could combine external data such as the telescope elevation, the temperature, the focus shift, and CCD height variations to assist the PSF characterization. The following shows the first attempt in this direction.

We examined a series of 25 science exposures in the HSC-*r2* band which were taken sequentially over about one hour. All the while, the telescope pointed to a single survey field and the elevation was kept almost the same (68° to 61°). The natural seeing then was mostly stable (around $0.^{\prime}5$ in FWHM) but varied during this time. The seeing was estimated from the PSF size averaged over a central $6'$ radius of the field. We then calculated the expected PSF size as a function of the field position using the ray-tracing results convolved with the seeing so that the image size at the center matches with the observed value. We subtract the calculated PSF size from the observed PSF size and the residual maps are generated as shown in figure 29a. The image plane is divided into 100×100 grids and the averaged residual is calculated inside each grid. The exposure time of each image

is 150 s, except for three exposures (30 s) at the lower left-hand corner labeled “S.”

We first note that the residual pattern has been mostly fixed for an hour. This is encouraging because it indicates the stability of the imaging system, which will enable accurate PSF characterization. We show an average of all the 25 residual maps in figure 29b, where orthogonally aligned residual patterns are clearly visible. The orthogonal pattern suggests that this could be explained by the height variation of CCDs. In fact, when we compare figure 29b with figure 16, we notice a clear coincidence that the taller CCDs tend to have larger positive residuals. A global slope is seen from the lower right-hand corner to the upper left-hand corner. This suggests the existence of the focal plane tilt and that the best focus position is realized in proximity to the upper-left corner.

Another source of the residual would come from the field variation of natural seeing. The stronger residual of the lower left-hand corner image could be explained by the seeing variation because the exposure time of the image is shorter (30 s) than those of regular images (150 s).

Unfortunately, however, the fixed pattern seen on figure 29a is not always clearly visible. When we change the telescope elevation by large amount (say, $>10^\circ$), the residual pattern generally changes. It is sensitive to the subtle change of the attitude of the camera. We need more studies to fully understand the PSF. One example to demonstrate the difficulty of the problem is shown in figure 30. We occasionally observe this type of an asymmetric degradation of images at one quarter edge of the field of view. It seems that the location of the degraded area is fixed on the telescope coordinate. This could be explained if we had a local heat source inside the WFC, but we have not

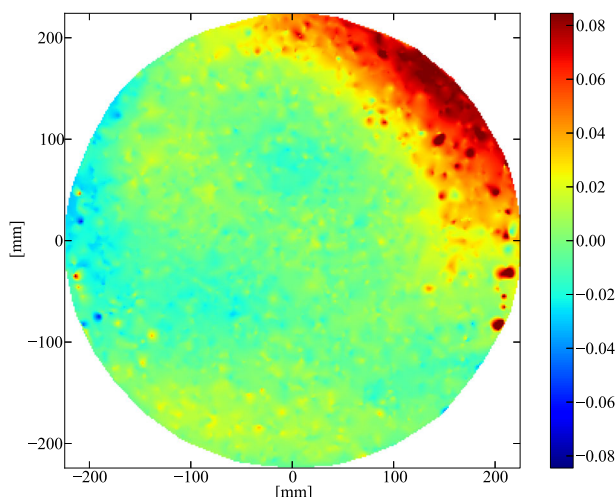


Fig. 30. Comparison of the amplitude of the small angular scale structure in the PSF map and the PSF correction error.

identified any such sources. Thus, the origin of the degradation is unidentified, which calls for more systematic studies. This is beyond the scope of this paper and draws our attention to the existence of problems in understanding and mapping the PSF.

7 Conclusion

We have designed and built a wide-field camera for the prime focus of the 8.2 m Subaru telescope, which we named “Hyper Suprime-Cam” (HSC). We estimated the image error components and verified the validity of some of the components through their dependence on the elevation and the instrument rotator angle. Overall, the achieved PSF is smaller than the accumulated worst-case estimated values and it is mostly limited by the natural seeing on Mauna Kea. Coupled with the large primary mirror and the wide field-of-view, HSC is one of the premier facilities for astronomical wide-field optical imaging in the world. Detailed analysis of the spatial variation of the PSF size suggests the

Table 10. Hyper Suprime-Cam in a nutshell.

WFC	Field of view	$\phi 1.5$ (497 mm)
	Focal length	18320 mm
	D_{80} in HSC- <i>i</i>	0''.23 ($EL = 30^\circ$ including design and manufacturing)
	Vignetting	25.6% max at the field edge
	Distortion	+3.19%
	Atmospheric Dispersion Corrector	Lateral-shift type
CCD	Type	Hamamatsu S10892-02 (HSC)
	Format	4176 × 2048 pixels
	Pixel size	15 μm (0''.169 at the field center)
	Number of CCDs	104 (+8 Focus CCDs and 4 Auto Guider CCDs)
	Quantum efficiency	400 nm 45% 600 nm 95% 800 nm 90% 1000 nm 40%
	Operating temperature	-100 $^\circ\text{C}$
Dewar	Dark current	a few e hr^{-1} pixel $^{-1}$
	Minimum interval between exposures	34 s (including wipe readout and save)
	Cooler	Two Pulse Tube Coolers (Fuji Electric)
	Cooling capacity	50 W each @ -100 $^\circ\text{C}$
Shutter	Cooler overhaul maintenance cycle	50000 hr
	Ion pump capacity	20 $\ell \text{ min}^{-1}$
	Aperture diameter	600 mm
	Minimum exposure time	2.0 s
Filter	Max deviation of the exposure time	0.01 s
	Physical diameter and clear aperture	600 and 580 mm
	Glass	Silica or B270
Filter exchanger	Thickness	13.7 and 15 mm
	Number of loadable filters	6
	Exchange time	14 min (+16 min for telescope setup)
Dimension	H 2972 mm, D _{max} 1827 mm, W _{max} 2278 mm (incl. FEU)	
Weight	Total 3490 kg (POPT2 1892 kg, WFC 893 kg, Camera Unit 385 kg, FEU 160 kg × 2)	

occasional occurrence of unexpected image deterioration. Further studies are necessary to identify the origins.

HSC began science operations on 2014 March and it has been used over 330 nights in its first three years, yielding about 43000 images to a total of 70 TB. Of those nights, 130 were allocated to the SSP program. We made the first public data release of the images and catalog taken in the first 1.7 yr (Aihara et al. 2017b) in which the field size in deg² (*r*-band 5 σ limiting magnitude) in Wide, Deep, and Ultra-Deep are 108 (26.4), 26 (26.6), and 4 (27.3), respectively. The survey will be completed by the end of 2019.

Table 10 summarizes the main characteristics of Hyper Suprime-Cam.

Acknowledgment

The Hyper Suprime-Cam (HSC) collaboration includes the astronomical communities of Japan and Taiwan, and Princeton University. The HSC instrumentation and software were developed by the National Astronomical Observatory of Japan (NAOJ), the Kavli Institute for the Physics and Mathematics of the Universe (Kavli IPMU), the University of Tokyo, the High Energy Accelerator Research Organization (KEK), the Academia Sinica Institute for Astronomy and Astrophysics in Taiwan (ASIAA), and Princeton University. Funding was contributed by the FIRST program from the Japanese Cabinet Office, the Ministry of Education, Culture, Sports, Science and Technology (MEXT), the Japan Society for the Promotion of Science (JSPS), Japan Science and Technology Agency (JST), the Toray Science Foundation, NAOJ, Kavli IPMU, KEK, ASIAA, and Princeton University. HM is supported by the Jet Propulsion Laboratory, California Institute of Technology, under a contract with the National Aeronautics and Space Administration. We thank the LSST Project for making their code available as free software at (<http://dm.lsst.org>).

Based on data collected at the Subaru Telescope and retrieved from the HSC data archive system, which is operated by Subaru Telescope and Astronomy Data Center at National Astronomical Observatory of Japan.

This work is in part supported by as MEXT Grant-in-Aid for Scientific Research on Innovative Areas (15H05892, 15H05887, 15H05893, 15K21733).

References

- Aihara, H., et al. 2017a, PASJ, in press (doi:10.1093/pasj/psx066)
- Aihara, H., et al. 2017b, PASJ, in press (doi:10.1093/pasj/psx081)
- Boulade, O., et al. 2003, SPIE Proc., 4841, 72
- Ezaki, Y., & Endo, M. 2014, Mitsubishi Denki Gihō, 88(2), 115
- Flaugher, B., et al. 2015, AJ, 150, 150
- Fukugita, M., Ichikawa, T., Gunn, J. E., Doi, M., Shimasaku, K., & Schneider, D. P. 1996, AJ, 111, 1748
- Gunn, J. E., et al. 1998, AJ, 116, 3040
- Imoto, H., et al. 2014, in Proc. 15th International Conference on Precision Engineering (Tokyo: Japan Society for Precision Engineering), C06, 299
- Iye, M., et al. 2004, PASJ, 56, 381
- Janesick, J. R. 2001, Scientific Charge-Coupled Devices (Bellingham, WA: SPIE), 255
- Kamata, Y., et al. 2006, SPIE Proc., 6276, 62761U
- Kamata, Y., et al. 2008, SPIE Proc., 7021, 70211S
- Kamata, Y., et al. 2012, SPIE Proc., 8453, 84531X
- Kamata, Y., Miyazaki, S., Muramatsu, M., Suzuki, H., Miyaguchi, K., Tsuru, T. G., Takagi, S., & Miyata, E. 2004, SPIE Proc., 5499, 210
- Kamata, Y., Miyazaki, S., Nakaya, H., Suzuki, H., Miyazaki, Y., & Muramatsu, M. 2010, SPIE Proc., 7742, 774229
- Kamata, Y., Nakaya, H., Kawanomoto, S., & Miyazaki, S. 2014, SPIE Proc., 9154, 91541Z
- Komiya, Y., et al. 2010, SPIE Proc., 7735, 77353F
- Komiya, Y. 2017, PASJ, in press (doi:10.1093/pasj/psx078)
- Komiya, Y., Miyazaki, S., Doi, Y., Nakaya, H., Furusawa, H., Takeshi, K., & Nariai, K. 2006, SPIE Proc., 6269, 62693E
- Massey, R., Stoughton, C., Leauthaud, A., Rhodes, J., Koekemoer, A., Ellis, R., & Shaghoulian, E. 2010, MNRAS, 401, 371
- Matsuda, T., et al. 2010, Abstract, 9th Int. Conf. on Optics-photonics Design and Fabrication (Tokyo: Optical Society of Japan), 19S1-09
- Miyatake, H., Fujimori, H., Aihara, H., Mineo, S., Miyazaki, S., Nakaya, H., & Uchida, T. 2012, IEEE Trans. Nuclear Science, 59, 1767
- Miyazaki, S., et al. 2002, PASJ, 54, 833
- Morokuma, T., Komiya, Y., Miyazaki, S., Nakaya, H., Furusawa, H., Tomono, D., Kawanomoto, S., & Tanaka, Y. 2008, SPIE Proc., 7014, 70144W
- Nakata, F., Miyazaki, S., Okada, N., Kimura, M., & Sekiguchi, M. 2000, in Proc. Optical Detectors for Astronomy II: State-of-the-Art at the Turn of the Millennium, ed. P. Amico & J. W. Beletic (Dordrecht: Kluwer Academic Publishers), 133
- Nakaya, H. 2012, PASP, 124, 485
- Nakaya, H., et al. 2008, SPIE Proc., 7014, 70144X
- Nakaya, H., et al. 2010, SPIE Proc., 7735, 77352P
- Nakaya, H., et al. 2012, SPIE Proc., 8453, 84532R
- Nakaya, H., Doi, Y., Kamata, Y., Komiya, Y., & Miyazaki, S. 2006, SPIE Proc., 6269, 62693G
- Nariai, K. 1992, Publ. Natl. Astron. Obs. Jpn., 2, 557
- Nariai, K., Yamashita, Y., & Nakagiri, M. 1985, Ann. Tokyo Astron. Obs., 20, 431
- Negishi, M. 2001, J. Jpn. Soc. Precision Eng., 67, 1632
- Obuchi, Y., et al. 2012, SPIE Proc., 8446, 84466Q
- Perlmutter, S., et al. 1998, Nature, 391, 51
- Riess, A. G., et al. 1998, AJ, 116, 1009
- Roddier, F. 1981, Prog. Optics, 19, 281
- Sekiguchi, M., Iwashita, H., Doi, M., Kashikawa, N., & Okamura, S. 1992, PASP, 104, 744
- Suzuki, H., Muramatsu, M., Yamamoto, K., Miyazaki, S., & Kamata, Y. 2007, in Proc. Nuclear Science Symp. Conf. Record, 2007 (New York: IEEE), 6, 4581
- Takeshi, K. 2000, PhD thesis, Mitaka, Tokyo: The Graduate University for Advanced Studies
- Uchida, T. 2008, IEEE Trans. Nuclear Science, 55, 1631
- Uchida, T., et al. 2012, SPIE Proc., 7014, 238
- Uraguchi, F., et al. 2012, SPIE Proc., 8446, 844663
- Weinberg, D., et al. 2013, arXiv:1309.5380
- Wynne, C. G. 1968, ApJ, 152, 675
- Yokota, H. 2001, J. Jpn. Soc. Precision Eng., 67, 1575